

A solid-state joining approach to manufacture of transition joints for high integrity applications

Himanshu Lalvani^{a,1}, Paranjayee Mandal^{a,2,*}, Anas Yaghi^{b,3}, Pedro Santos^{b,4}, Bernd Baufeld^{c,5}

himanshu.lalvani@strath.ac.uk¹; paranjayee.mandal@strath.ac.uk²; anasyaghi@hotmail.com³;
pedro.santos@the-mtc.org⁴; Bernd.Baufeld@pro-beam.com⁵

^a*Advanced Forming Research Centre, National Manufacturing Institute of Scotland, University of Strathclyde,
85 Inchinnan Drive, PA4 9LJ, UK*

^b*MTC Limited, Ansty Part, Coventry, CV7 9JU, UK*

^c*Pro-beam technologies GmbH, Zeppelinstr. 26, 82205 Gilching, Deutschland*

*Corresponding author, ORCID id: 0000-0002-8440-703X

Abstract

Manufacture of a transition hybrid coupling from two different steels, medium carbon S355J2 and stainless 316L, has been demonstrated using two different solid-state joining routes, forge welding (FW) and rotary friction welding (RFW). An additional manufacturing route, electron beam welding (EBW), was also employed in investigating its feasibility for such application. Mechanical and microstructure properties of the final components manufactured from the three different routes have been compared. Finite element (FE) analysis was utilised to determine optimal geometries for the FW and the RFW preform rings and identify optimal parameters for both processes. Of the three manufacture routes, the FW produced an instant diffusion-like bond with a single forging stroke on a 2100T screw press with the thinnest weld interface and most uniform hardness distribution at either side of the joint. The RFW part, manufactured on a 125T RFW machine, also exhibited a very thin weld interface, yet slightly thicker compared to the FW case, with small variations in the hardness distribution at either side. The EBW produced markedly thicker weld interface compared to the two solid-state routes. The EBW part exhibited significant variation in hardness distribution across the weld exhibiting peak hardness in the weld indicating requirements for a post-weld heat treatment (PWHT). Both the FW and the RFW process routes exhibited very uniform micro-hardness and microstructures across the weld interface in contrast with the EBW process in as-manufactured condition.

Keywords:

Forge welding (FW); rotary friction welding (RFW); electron beam welding (EBW); mechanical properties; microstructure; finite element (FE) modelling

1. Introduction

Dissimilar metal joints are used in nuclear, oil and gas, energy, chemical processing and many other sectors due to a combination of desired properties they offer for complex and high integrity applications. In nuclear power plants the reactor pressure vessel (RPV) are made of low alloy steels and the main pipe line material is normally stainless steel requiring a dissimilar weld at the intersection between the RPV and the main pipe lines. A transition piece, also called safe-ends, is required to facilitate assembly welding between the RPV and the stainless steel piping. Normally, such transition pieces are manufactured from stainless steel or nickel-base alloy (e.g. Alloy 600) and are welded to the RPV in the manufacturing shop. The final assembly weld between the RPV (including the transition piece) and the stainless piping is carried out in the field. Such dissimilar welds require multi-pass or buttering welds to achieve desired properties and reduce susceptibility to environmental assisted cracking and stress corrosion cracking. The safe-end transitions are complex to manufacture and require multiple layers of welds (buttering) with carefully chosen filler materials to ensure safe operation in critical environments [1]. In an extensive review of dissimilar welds between martensitic and austenitic steels in power plant applications, the issues encountered in joining of such steels using conventional arc welding route and the complexities of choosing different fillers for mitigating them was discussed in detail [2]. Challenges of dissimilar steel welds fabricated with conventional arc welding methods include mismatch in thermal expansion coefficient resulting in residual stresses, post-weld heat treatments causing carbon depletion and migration, sensitization and susceptibility to creep damage due to the carbon depletion zones, hot-cracking and formation brittle intermetallic compounds to name a few [2], [3]. In another in-depth study of joining SS 304 and medium carbon EN8 steel via tungsten inert gas (TIG) welding process, a range of complex microstructures resulting from varying weld parameters were discussed in detail [4].

A transition piece manufactured from two different metals using solid-state joining techniques can provide a robust and simpler solution for the challenges faced during manufacture of safe-ends by conventional arc welding of dissimilar metals requiring complex multi-weld routines with multiple and carefully selected fillers. For example, joining of AISI 304 austenitic stainless steel and AISI 430 ferritic stainless steel has been studied using continuous drive RFW and the toughness and strength of austenitic–ferritic stainless steel welds are found better than the parent ferritic steel with deformation observed only being confined to it [5]. The continuous drive RFW has also been employed to join forged and cast AISI 1050 and AISI 304 steel pairs, where process optimisation has been carried out in order to maximise tensile strength for both forged and cast pairs. As the ability of friction welding depends on the material forgeability, thus the friction welded forged parts show higher tensile strength but lower hardness as compared to the cast parts. The weld zone shows recrystallized regions with presence of

some martensitic laths formed during welding [6]. HIP diffusion bonding has been studied for many alloy combinations, however joining large-size diverter attachment fittings (total structural assembly mass of 760 kg and the diffusion bonded surface area is in the range of 770 – 1260 cm²) made of corrosion-resistant AISI 316L stainless steel and high-strength XM19 steel has attracted attention. The HIP diffusion bonding zone shows absence of oxide phases in the weld zone and high tensile strength than 316L steel, therefore the tensile failure is observed outside the diffusion bonding zone of 316L steel [7]. Another method for efficient joining of ferritic and austenitic steels is use of functionally graded materials (FGM) produced via additive manufacturing technique. It has been observed that the layered composition grading fabricated by laser-based directed energy deposition (DED) can effectively join 2.25Cr-1Mo steel and 800H alloy steel pairs and PWHT can prevent the carbon loss due to diffusion from the ferritic steel under service conditions. The microstructure of the composition grading shows a gradual change from martensitic to fully austenitic structure. The austenitic region lacks any substantial resistance to carbon diffusion, which is benefitted by the application of PWHT [8].

Punshon et al. [9] demonstrated manufacture of a transition coupling using single pass EBW followed by drop forging process. They utilised the forge welding manufacturing route to join SA508 steel to 304SS and to Inconel 600. The process involved joining of dissimilar raw material blocks using EBW with single pass to keep the blocks intact followed by multiple strokes on drop hammer forge to create a forge weld at the interface. The hybrid work piece was then forged radially to create a disk shape followed by piercing a hole in the middle to produce a hybrid hollow coupling. Their approach showed promising results with satisfactory mechanical properties of the joint as well as ultra-sonic tests to show defect free final joint. Finally, the standard and most commercial application of EBW is related to steels, but it can be successful to weld a number of dissimilar metals unless forming brittle intermetallic components in the transition zone. Due to the use of vacuum, EBW produces a clean joint and doesn't suffer from oxidation and other impurities as in the case of arc welding and also has a much narrower weld and heat affected zone (HAZ) due to high energy density. This high energy density also enables thicker sheets to be joined but simultaneously leads to a significant temperature gradient in the weld zone as compared to any other welding methods. It has been proved that EBW can be effectively implemented in single track joining of 100 mm thick coupons of SA508 grade 3 and grade 4N steels. Although no defects are identified in the weld zone, however mismatch in hardness and tensile strength properties of the parent materials and the weld indicates necessity of PWHT [10].

The current work focuses on demonstrating feasibility of the FW and the RFW process in manufacture of a hybrid transition coupling from two different steels, medium carbon S355J2 and stainless 316L. An additional manufacturing route, EBW, has also been employed to understand the benefit of the FW and RFW routes over EBW route. Appropriate simulation work was undertaken using the commercial FE software DEFORM to determine – (i) maximum employable diameter for the preform rings to fit

on the available die block set for the FW process and (ii) to determine **optimal forging stroke or upset for producing good quality weld and avoiding excessive flash generation** during RFW. Novelty of the current work lies in the utilisation of the three manufacture routes employed in this work to demonstrate manufacture of hybrid transition couplings and appropriate FE analysis, mechanical and microstructure characterisation to determine suitability of these processes for the said application.

2. Materials and Manufacturing Routes

2.1 Materials

Structural grade S355J2 medium carbon steel is a micro alloyed steel suitable for mechanical engineering applications. It has good weldability with a maximum carbon equivalent of 0.47 for all variants [11]. Austenitic 316L stainless steel (316L SS) is a standard molybdenum-bearing grade (molybdenum provides better overall corrosion resistant properties than 304 grade) with excellent formability and weldability. It is widely used in various industries including construction and transportation. In this work, the supply condition of the both S355J2 and 316L SS was hot-rolled hollow bars supplied in lengths of 3 meters with OD of 150 ± 1.5 mm and ID of 106 ± 1.1 mm. The chemical compositions of the as-received bars are listed in Table 1. Both the hollow bars were saw cut into several long pieces (109 mm length for RFW process and 40 mm length for both FW and EBW processes) and the ID of each pieces was then precisely machined to 105 ± 0.1 mm in order to accurately join the dissimilar metal rings together. These machined metal rings were then used to make preforms, through seal welds, for all three manufacturing routes.

Table 1: Chemical composition of the as-received S355J2 steel and 316L SS

S355J2 steel	Element	C	Mn	P	S	Cr	Ni	Mo	N
	Wt%	0.18	1.33	0.014	0.001	0.04	0.09	0.01	0.008
	Element	Si	Cu	Al	Nb	Ti	V	Fe	
	Wt%	0.2	0.21	0.024	0.001	0.001	0.021	balance	
316L SS	Element	C	Mn	P	S	Cr	Ni	Mo	N
	Wt%	0.013	1.47	0.022	0.027	16.9	11.35	2.1	0.06
	Element	Si	Fe						
	Wt%	0.49	balance						

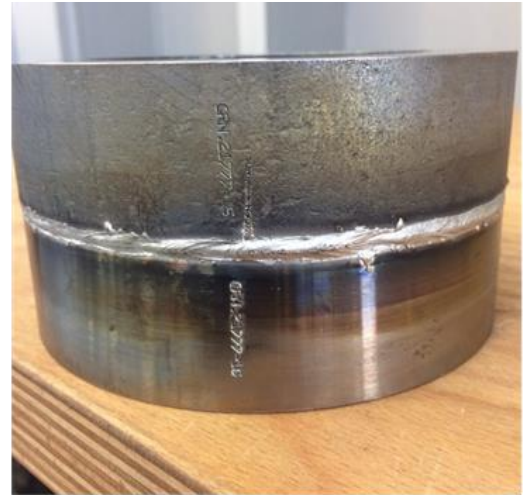
2.2 Forge Welding (FW)

Forge welding is one of the simplest and oldest joining methods that is very effective in producing high quality solid-state joints. The process involves forging of similar or dissimilar metals at relevant hot forging temperatures to produce an instant diffusion bond. The process has apparent advantage over conventional diffusion bonding process in that the former produces instant bond whereas the later takes several hours, for a large boning area, to produce a sound joint. However, the use of this process in

manufacturing hybrid parts has been scarce possibly due to expensive equipment compared to conventional joining equipment. A superior weld quality was reported during forge welding between SS 316L and AA6063 alloy as compared to similar joints produced with friction welding and diffusion bonding processes [12]. In this study, machined S355J2 and 316L SS rings, each 40 mm in length (Figure 1a) were seal welded together to produce preforms (Figure 1b) for FW process using two different welding methods – (i) GTAW and (ii) EBW. Both the methods used 2 mm deep seal welding at OD and ID sides of the rings, which accurately stacked the two rings together as a hybrid ring preform. Except the small seal welded area at the OD and ID sides, the rest of the interface between two dissimilar rings was left to be joined, in solid-state, during forging. The seal welding served two purposes – (i) it kept the two rings intact during furnace loading and transfer to the forge and (ii) it created a vacuum seal to prevent oxidation at the interface during heating. The hybrid ring preforms were then heated in a furnace at two different forging temperatures, 1050°C and 1100°C, for 2 hours to achieve homogeneous temperature distribution. The heated preforms were then transferred to the lower flat die (Figure 1c), kept at 400°C, of the 2100T screw press and forged with a single blow (Figure 1d), at two different height reductions of 25% and 37.5%. These height reductions led to final forging height of 60 mm and 50 mm respectively from initial hybrid preform height of 80 mm (Figure 1e). A of total 12 hybrid preforms were forged at different forging parameters as listed in Table 2 to include two different temperatures, two different height reductions and also taking into account the orientation of preform placed on the lower die (i.e. either placing 316L SS side or S355 side on the lower die). It was found that only 50% of the screw press energy was sufficient to produce a 37.5% height reduction. For each forging operation, the die blocks were lubricated with graphite suspension in water, called DAG, and then dies were cleaned and re-lubricated in between each forging run. The forging operation created an instant diffusion-like bond at the interface between two dissimilar rings of the hybrid preform. Following each forging operation, the FW parts were air-cooled. The air-cooled parts were proof machined to produce final transition hybrid coupling demonstrator part (Figure 1f). The proof machined hybrid ring was then tested using ultrasound technique for any defects at the interface. In this case, the ultrasound inspection revealed no defects at the forge weld interface. All the FW parts exhibited better mechanical properties than parent materials at the weld confirmed by tensile specimens that failed away from the weld-line. The FW-02 and the FW-09 were selected amongst the batch for further mechanical and microstructural analysis as both were forged at lower temperature (i.e. lower energy consumption cases) and incorporated each type of seal weld in the preform, i.e. GTAW and EBW.



(a)



(b)



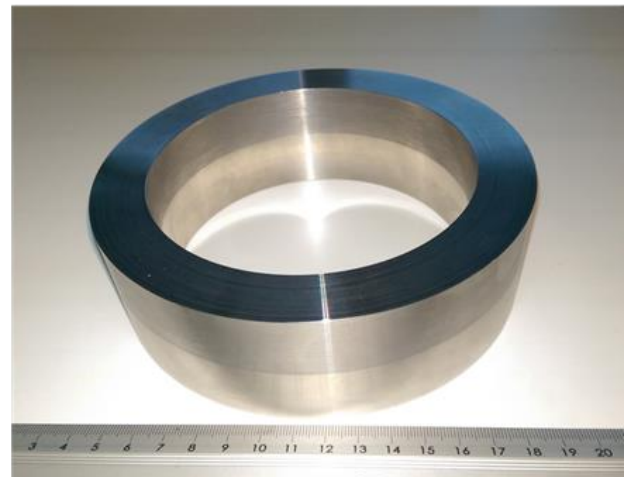
(c)



(d)



(e)



(f)

Figure 1: Schematic diagram of the forge welding (FW) process as adopted in this work – (a) machined S355J2 and 316L SS rings of 40 mm height, (b) GTAW and EBW seal welded hybrid preforms of 80 mm initial height, (c) heated hybrid preform of 80 mm height prior to forging, (d) hybrid preform just after forging – forged product with 50 mm final height, (e) forge welded ring after air cooling, (f) proof machined forged welded final part

Table 2: Forge welding process parameters. The bold lines indicate selected forge welded discs for further study.

Forge welded sample ID	Seal weld type	Forging Temperature (°C)	Screw press energy (%) Input	Height reduction (% of initial height)	Preform placement on screw press
FW-01	GTAW	1050	90	25	S355J2 on lower die
FW-02	GTAW	1050	75	25	316L SS on lower die
FW-03	GTAW	1100	60	25	316L SS on lower die
FW-04	GTAW	1100	50	25	316L SS on lower die
FW-05	GTAW	1100	50	25	316L SS on lower die
FW-06	EBW	1100	50	25	316L SS on lower die
FW-07	EBW	1100	50	25	S355J2 on lower die
FW-08	EBW	1100	60	25	316L SS on lower die
FW-09	EBW	1050	50	25	316L SS on lower die
FW-10	GTAW	1100	50	37.5	316L SS on lower die
FW-11	EBW	1100	50	37.5	316L SS on lower die
FW-12	EBW	1100	50	37.5	316L SS on lower die

2.3 Rotary Friction Welding (RFW)

Rotary friction welding uses both friction and compressive axial forces to join two dissimilar metal parts, where one part rotates at high RPMs relative to another which is kept stationary. The two parts are perfectly aligned coaxially. This process accelerates one of the parts to the target speed and then presses both the parts together to generate friction, which in turn produces enough heat for the metal parts to plasticise and then to form a bond or weld between them. The advantage of RFW is that it produces a much narrower HAZ compared to the fusion welding counter-part, with the benefit of maintaining favourable material properties at the interface as there is no melting involved. There are two primary variants for RFW; continuous drive friction welding (CDFW) and inertia friction welding (IFW). This study utilises the second approach, where the flywheel is attached to the rotating side of the machine in order to increase the moment of inertia, and therefore controls the amount of energy going into the weld interface. The quality of the weld can be assessed based on the amount of the weld flash, total reduction in part length due to the formation of flash and cross-section metallurgical analysis. In this study, the machined S355J2 and 316L SS rings, each of 109 mm height, were prepared for RFW process by making required key-way slots at one of the ends for locking the parts, against each other, at two ends of the machine. In order to ensure the precision and the repeatability of the RFW process, total 13 RFW rings were produced using different welding parameters as listed in Table 3. Parameters were chosen based on past experience with similar material joining of other steels and a design of experiment (DoE)-like approach for the speed and pressure parameters. The major input process variables observed during RFW were the inertia, pressure and rotation speed, whereas the output was measured using machine upset, i.e. total reduction in final part length. Figure 2 shows various images (a-d) from the RFW trials conducted in the current study. Figure 3a shows a selected RFW part, i.e.

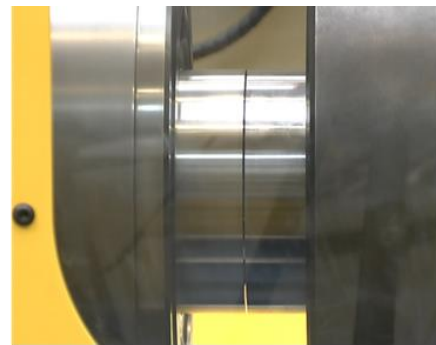
RFW-12, with key-way slots and Figure 3b shows a full longitudinal cross-section. Figure 3c and Figure 3d shows the samples extracted for tensile, microstructure and hardness analyses from the longitudinal cross-sections. RFW-12 was finally proof machined to produce transition hybrid coupling demonstrator parts as observed in Figure 3e. All the RFW parts exhibited better mechanical properties as confirmed by the tensile tests that failed away from the weld-line, but only RFW-12, manufactured using optimised parameters, was selected for further analysis.

Table 3: Rotary friction welding process parameters. The bold lines indicate selected friction welded discs for further study.

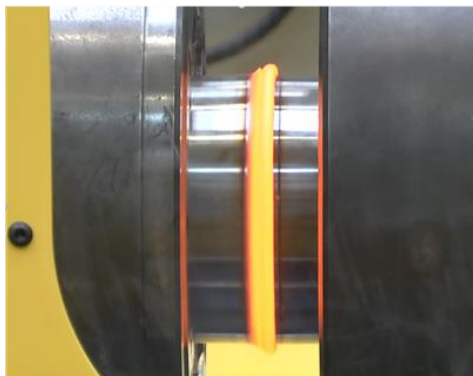
RFW sample ID	Input			Output
	Inertia (kg.m ²)	Rotational Speed (RPM)	Pressure (bar)	Machine upset (mm)
RFW-1	168.6	1010.5	293	8.12
RFW-2	168.6	846.5	293	3.65
RFW-3	168.6	1148.07	293	14.1
RFW-4	168.6	1009.85	196.92	4.39
RFW-5	168.6	1209	196.92	10.27
RFW-6	168.6	1209	260.97	14.63
RFW-7	268.6	746.17	260.97	5.34
RFW-8	268.6	786.06	260.97	6.9
RFW-9	268.6	786.06	289.92	8.18
RFW-10	168.6	1010.5	293	7.95
RFW-11	168.6	1010.5	293	8.41
RFW-12	168.6	1010.5	293	8.26
RFW-13	168.6	1010.5	293	8.36



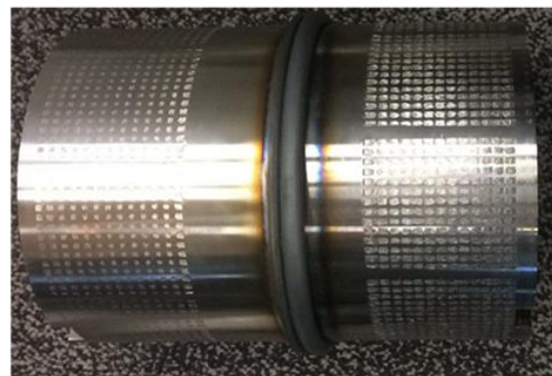
(a)



(b)



(c)



(d)

Figure 2: Images from the rotary friction welding (RFW) trials conducted in this work – (a) machined 316L SS and S355J2 rings of 109 mm height, (b) machined rings ready for rotary friction welding, (c) during rotary friction welding of dissimilar metal rings, (d) rotary friction welded dissimilar metal rings

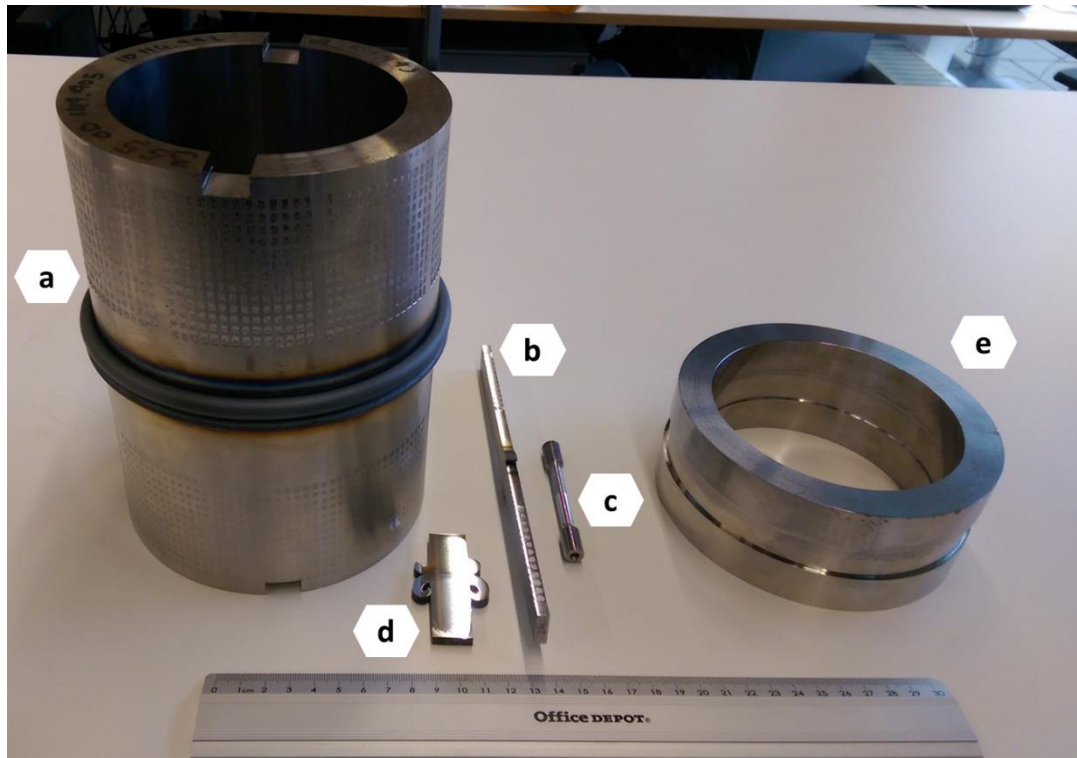


Figure 3: RFW-12 – (a) after rotary friction welding, (b) a full longitudinal cross section, (c) round tensile sample extracted from the longitudinal cross section, (d) longitudinal cross section prepared for microstructure and hardness testing, and (e) final proof machined component

2.4 Electron Beam Welding (EBW)

Electron beam welding involves joining of metallic materials by melting the area of a welded joint, with the aid of an electron beam gun, in high vacuum in the range from 10^3 to 10^6 mbar, in a medium or reduced vacuum from 75 to 1000 mbar, with or without vacuum [13]. The EBW has several advantages over conventional fusion arc welding, particularly for dissimilar welding, such as accurately controllable and high energy density making it capable to weld very thin sheets to very thick metal parts (up to 300mm for steels and 500mm for aluminium), low heat input per unit length producing thin weld bead and HAZ, vacuum environment eliminating contamination and oxidation issues and more. The process does have its disadvantages such as limitation on part sizes due to requirement of vacuum chamber, beam deflection due to difference in magnetic properties of dissimilar metal, weld porosity and brittleness due to rapid solidification [14]. In the current work, two precisely machined faces of S355J2 and 316L SS rings were put together to prepare a radial butt joint and a full penetration EBW was carried out in ProBeam K25 EBW chamber with a beam current of 100 mA, velocity of 6 mm/s

and working pressure of ~ 3 mbar resulting in a through thickness welded transition hybrid coupling demonstrator as shown in Figure 4.

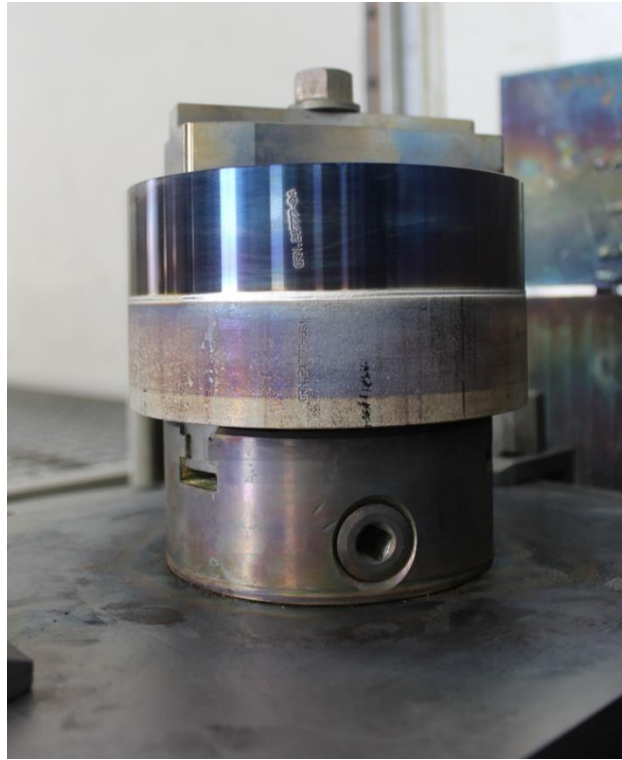


Figure 4: As-manufactured EBW ring with full penetration (or through thickness) weld (top is 316L SS and bottom is S355J2)

3. Process Modelling

Both RFW and FW processes were simulated with the finite element (FE) method, using the commercial software DEFORM. It has the advantage of re-meshing automatically as large deformation takes place, which is critical for such type of FE modelling. The FE modelling provided guidance on key process parameters for both processes. For the FW process, it was vital to determine maximum employable diameter for the preform rings such that when the preforms are forged the outward expansion of the ring preform assembly remains within the die block boundary. Moreover, FE analysis provided insight into different levels of deformation and bulging occurring when the ring preform assembly containing two different steels is forged at high speeds on the screw press helping to determine optimal level of forging stroke to be selected. For the RFW process, it was useful to determine [optimal process parameters such as RPM and forging stroke \(or upset\) to produce a good quality weld and to avoid excessive flash generation](#). Both process models have been executed with an error falling within 10% of the realistic process conditions.

3.1 FE Modelling of the RFW Process

The process of inertia RFW of dissimilar S355 and 316L steel tubes using the 125T machine was generally controlled by specifying the axial pressure, rotational velocity and required moment of inertia of the flywheels. The input welding parameters of the machine are – (i) the moment of inertia (provided by a combination of flywheels), (ii) the angular speed of the rotating part (including the flywheel) and (iii) the axial force (pushing the components to be welded together). The control parameters, as shown in Table 3, are set with the intention to produce a “good weld”, which is loosely defined (from practical experience of the weld experts at the MTC) as a weld that has been produced with an upset of between 45% and 55% of the wall thickness of a welded tube. The upsetting of the dissimilar steel tubes during RFW was in the axial direction and this resulted into the emergence of a flash due to conservation of mass.

3.1.1 Generation of FE Model and FE mesh

The steel tubes had the length of 106 mm, outer diameter of 150 mm and wall thickness of 17.5 mm. Among the 13 sets of dissimilar welded tubes named RFW1 – RFW13, 9 sets comprised a range of welded trials that were used to calibrate and validate the FE model, and 4 sets comprised actual “good welds” that further validated the FE model and were designated for future metallurgical testing. The FE model was two-dimensional (2D) and axisymmetric. It was a torsional type of model, allowing torsional stresses and strains to occur in the circumferential direction. The type of simulation was Lagrangian and incremental. It was thermo-mechanically coupled, and hence it calculated deformation and heat transfer concurrently. The parts of the machine in contact with the tubes were made rigid in the simulation, whereas the tubes were assigned plastic properties. Each simulation was run over 1550 steps, with each step lasting 0.01s. The maximum allowed strain in each element was limited to 0.1. The iteration method was specified as Newton-Raphson. The environment temperature was set as 20°C. Von Mises yield criterion and the isotropic hardening rule were assumed. The RFW machine efficiency was specified to be 90% in the FE simulations. The relationship between the heat generated at the weld interface, the machine efficiency (ξ), the moment of inertia (I) and the angular speed (ω) is given in the following equation, as specified in the DEFORM manual V11.1:

$$\text{Equation 1: Heat Generated} = \xi I \omega^2 / 2$$

Figure 5 shows the generated FE mesh, which was refined at the weld interface to accurately model the flash formation during welding. The mesh of the S355 model contained 2125 elements and 2241 nodes, and the mesh of the 316L model contained 1995 elements and 2112 nodes. Re-meshing was triggered at an interference depth of 0.05 mm. All the elements in the simulations were linear.

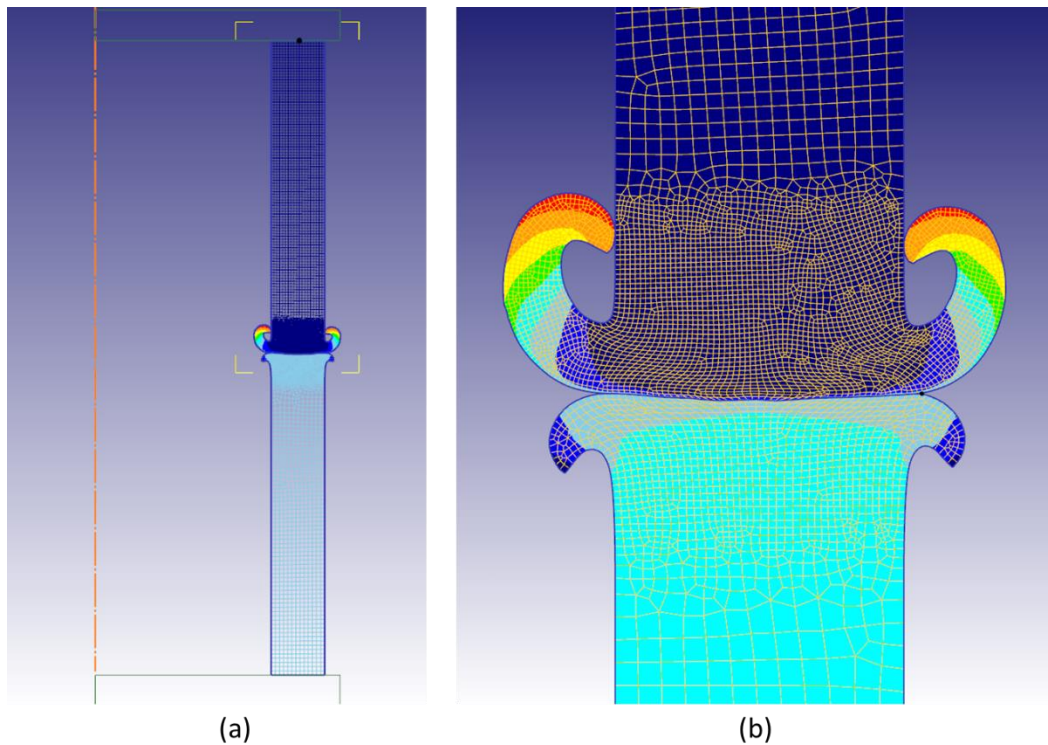


Figure 5: (a) FE model showing the tube axis in orange and overall mesh of the upper S355 steel tube and lower 316L stainless steel tube and (b) a zoom-in of the refined part of the meshes at the weld interface.

3.1.2 Material Property Data

Although the material library in DEFORM had flow stress data for the two types of utilised steel, covering the temperature range from 20°C to 1370°C, and the strain rates of 1s^{-1} and 50s^{-1} , the stress flow curves were not entirely consistent, crossing one another at points where no cross over was expected. The initial simulations using the flow stress data in DEFORM didn't give satisfactory results, particularly the degree of upset expected for the given welding parameters and conditions. Therefore, a set of flow stress data for the same temperature and strain rate ranges stated above was derived from a number of publications [15], [16], [17] as well as by referring to general trends of behaviour of steel as specified in the DEFORM material library and elsewhere [18]. The derived stress flow curves are provided as supplementary information. The other material property data used in the FE simulations for both types of steel, obtained from the DEFORM material library and extrapolated when necessary by referring to steel trends of behaviour expressed elsewhere [19]. Poisson's ratio was specified as 0.3 and radiation emissivity as 0.7 for both materials. Mass density for 316L and S355 materials was specified as 8000 kg/m^3 and 8780 kg/m^3 respectively. Young's modulus for S355 was assumed constant at 210 GPa. The coefficient of friction was assumed to be 0.7 between the two tubes at the weld interface [20]. Heat losses at free surfaces were prescribed as specified in literature [19]. For both materials, the Young's modulus, thermal expansion, thermal conductivity and heat capacity as a function of temperature are provided as supplementary information.

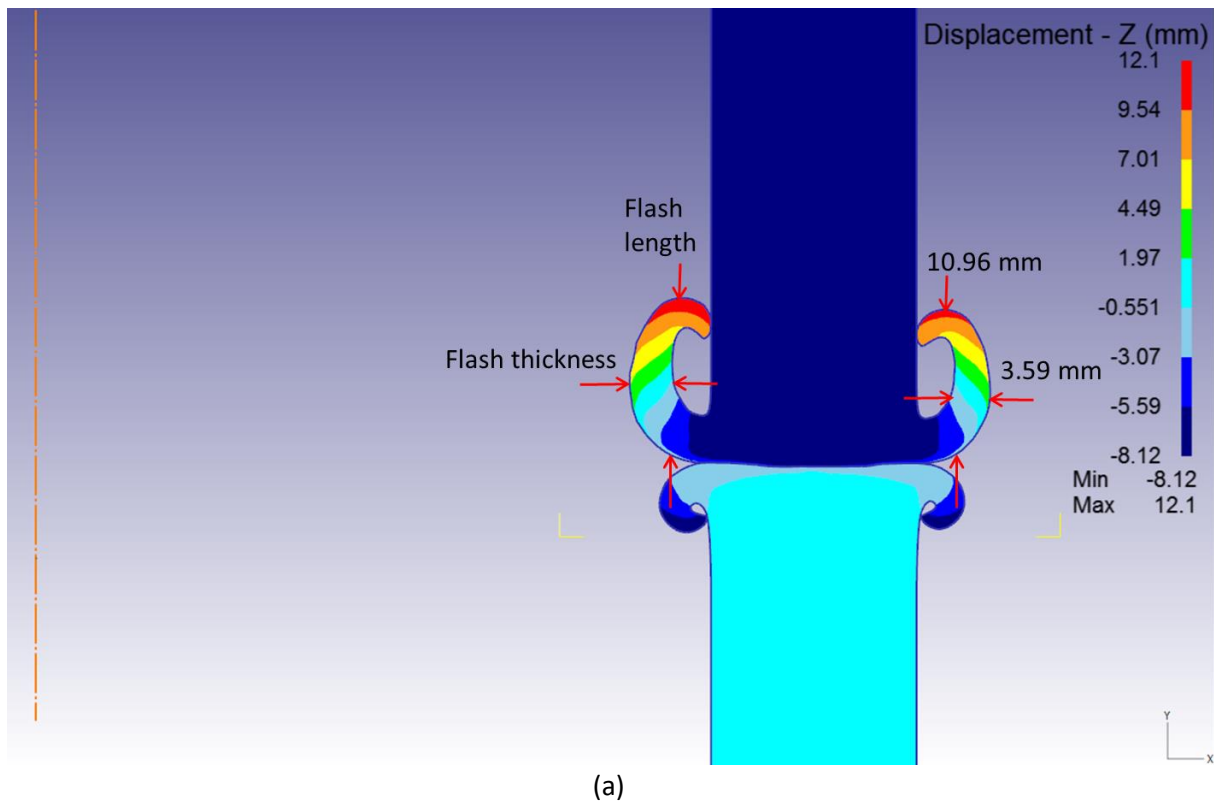
3.1.3 FE Results and Comparison with Experimental Measurements

Table 4 shows the FE predicted and experimentally measured total upset, together with the percentage error and the ratio of measured upset /wall thickness for all 13 RFW trials. The FE models including the implemented material property data were calibrated using the experimentally measured upset of a weld that was considered to be a “good weld”, i.e. model RFW1 in Table 4 and the ratio of upset /wall thickness for RFW1 is 46.4%. The same material property data were then used for all the remaining FE models. The FE results and the corresponding comparisons with the experimentally measured upset values presented in Table 4, show that the accuracy of the FE predictions drops significantly as the welding parameters move away from the optimum values for a “good weld”. The error in the FE upset plotted against the ratio of the actual upset over the wall thickness has been provided in the supplementary information section. A cross-sectional view of the RFW part is presented in Figure 6a, which shows heat-map of the displacement values, useful in visualising extent of the upset. From Table 4, it can be seen that the error values for RFW1 and RFW10 – RFW13 are very similar (all being zero or close to zero values) and the cross-sectional view shown in Figure 6a corresponds to all these parts. The flash generated as a result of the forging stroke/upset in the RFW process can be a good feature to provide a comparison between the simulated and the actual part to gauge the accuracy of the FE model. Therefore, flash length and thickness measurements are provided for a couple of parts with minimum and maximum error values to show differences between the simulated and the actual part cross-sectional views. A good agreement between the simulated and the actual cross-section views can be seen for the RFW2 and RFW13 parts (representing most and least FE upset errors respectively) confirming the accuracy of the FE model. For example, the flash length and thickness obtained from the RFW13 model are 10.96 mm and 3.59 mm respectively (Figure 6a), whereas the same measured from the actual RFW13 cross-section are 10.02 mm and 3.79 mm respectively (Figure 6b). Similarly, the flash length and thickness values acquired for RFW2 model are 8.2 mm and 3.32 mm respectively (Figure 7a), but are found as 7.51 mm and 3.64 mm respectively from the actual RFW2 cross-section (Figure 6b). Figure 7a – h further shows the cross-sectional views from simulation of different RFW parts, RFW2 to RFW9, corresponding to different upset values listed in Table 4. A maximum error of 44.1% resulted from the model of the RFW2 and the upset to wall thickness ratio was 20.86% indicating significant deviation from the experimental data. In contrast, for models RFW10 to RFW13, the error ranges between 2.1% and –3.4%. Of all the simulated welds in this work, six have upset values between 40% and 50% of the tube wall thickness, for which the error in the predicted upset falls within 10%. It has been reported in literature that, in general, the difference between modelling predictions and experimental measurements in welded components demonstrated an error ranging between 20% and 40% [21]. Further, the normalized upset in the case of 7 trials of RFW between dissimilar materials demonstrated a difference between modelling predictions and experimental measurements ranging between 5% and 45% [22]. It is however acknowledged here that, for an accurate FE model that can

deliver accurate results for a wide range of welding parameters, there is a need to carry out a detailed parametric study, the result of which may be an improvement in the modelling approach as well as the material property data.

Table 4: FE predicted and experimentally measured total upset, percentage error and the ratio of measured upset/wall thickness

RFW model no	Prescribed energy (N-mm)	Force (N)	FE angular speed (rpm)	Actual angular speed (rpm)	FE upset (mm)	Actual upset (mm)	Error in FE upset (%)	Actual upset (%)
RFW1	9.39E+08	1.24E+06	1007.85	1007.85	8.12	8.12	0	46.4
RFW2	6.61E+08	1.24E+06	845	844.23	5.26	3.65	44.1	20.86
RFW3	1.21E+09	1.24E+06	1146.07	1145.19	10.5	14.10	-25.5	80.57
RFW4	9.39E+08	8.3E+05	1007.85	1007.38	5.24	4.39	19.4	25.09
RFW5	1.35E+09	8.3E+05	1207	1188.83	7.96	10.27	-22.5	58.69
RFW6	1.35E+09	1.1E+06	1207	1206.07	10.5	14.63	-28.2	83.6
RFW7	8.2E+08	1.1E+06	746.17	744.15	7.09	5.34	32.8	30.51
RFW8	9.1E+08	1.1E+06	786.06	784.12	8.1	6.90	17.4	39.43
RFW9	9.1E+08	1.22E+06	786.06	784.08	8.98	8.18	9.8	46.74
RFW10	9.39E+08	1.24E+06	1007.85	1007.65	8.12	7.95	2.1	45.43
RFW11	9.39E+08	1.24E+06	1007.85	1007.69	8.12	8.41	-3.4	48.06
RFW12	9.39E+08	1.24E+06	1007.85	1007.61	8.12	8.26	-1.7	47.20
RFW13	9.39E+08	1.24E+06	1007.85	1007.77	8.12	8.36	-2.9	47.77



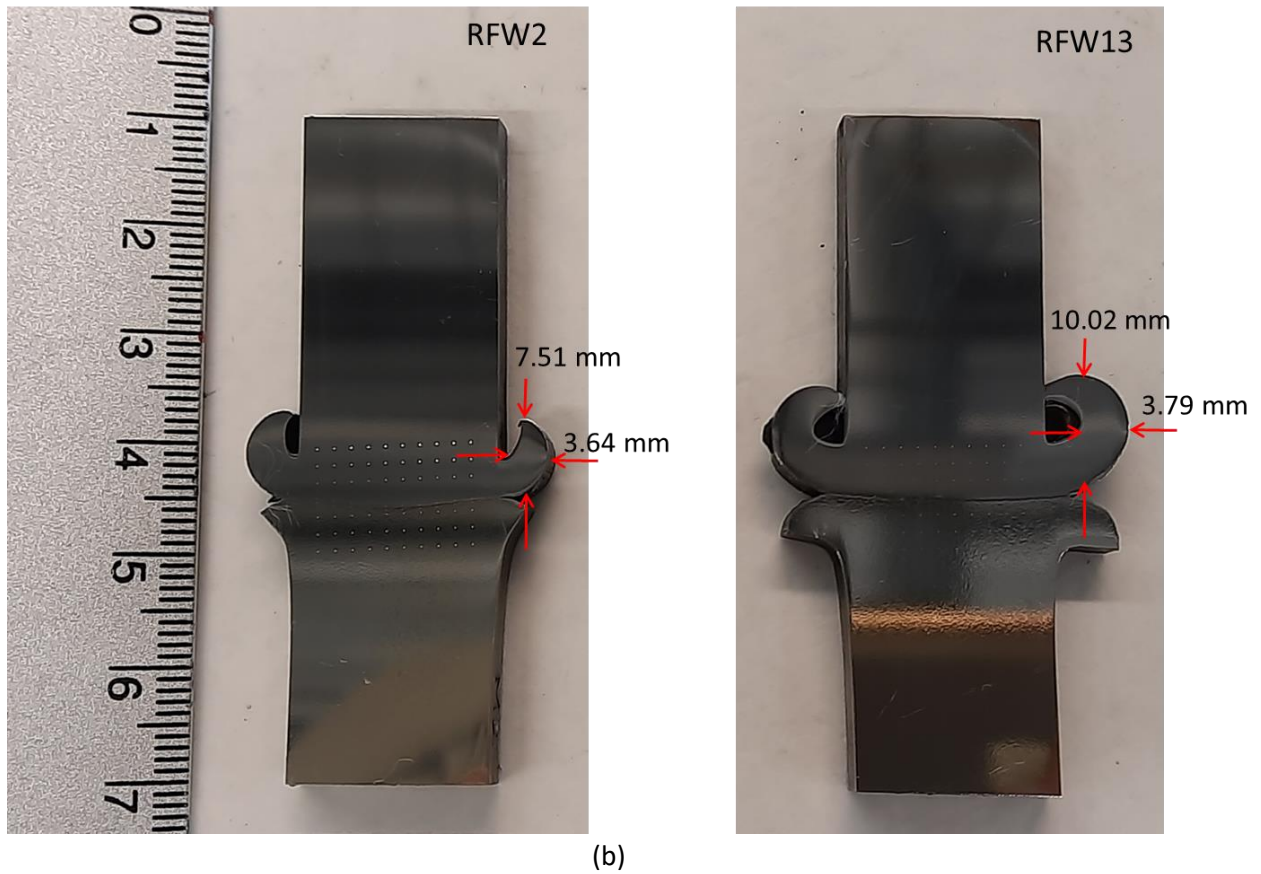


Figure 6: (a) Cross-sectional view of an RFW simulated part showing upset values (minimum vertical displacement) and the extent of flash generation (results showing simulations of RFW1 and RFW10 – RFW13) and (b) Images of weld cross-sections of RFW2 and RFW13 parts showing differences in extent of flash generation between the two cases.

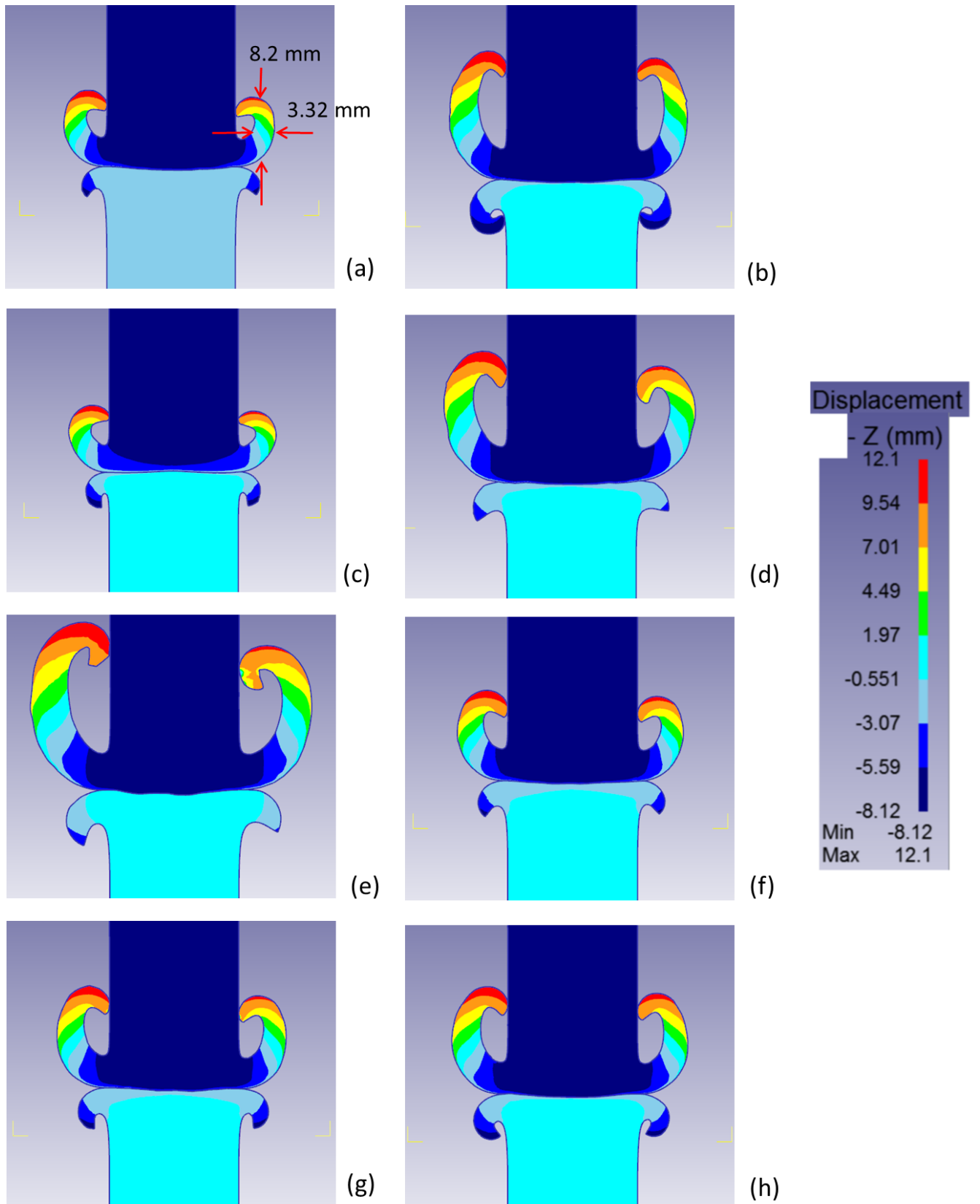


Figure 7: Images of RFW weld cross-sections, from simulations, showing different levels of upsets (a) RFW2 (comparison of flash length and thickness with the experimental one is provided in Figure 6b), (b) RFW3, (c) RFW4, (d) RFW5, (e) RFW6, (f) RFW7, (g) RFW8 and (h) RFW9 in FE models.

3.1.4 FE Parametric Studies

The parametric study considered the effect of changing the coefficient of friction on the upset value. Depending on temperature, the coefficient of friction for 316L can have a value between 0.35 and 0.70 for dry surface conditions [20]. The effect of the coefficient of friction on the FE upset value was investigated by running a series of simulations for model RFW1 by changing the coefficient of friction value from 0.35 to 0.95, the results of which are shown in Figure 8. This also shows that the effect of changing the coefficient of friction at the weld interface can have a significant effect on the FE upset value. Hence, to demonstrate how changing certain parameters could affect the FE upset value, models RFW2 – RFW6 had their coefficient of friction modified and the resulting FE upset values were obtained by carrying out further FE simulations. The resulting upset values corresponding to the modified coefficient of friction are shown in Table 5. The percentage errors range between 5.8% and -3.6%. It is worth noting that values for the coefficient of friction higher than 0.7 are probably not realistic, nonetheless this parametric exercise was done to demonstrate that better accuracy can be achieved by changing some property values.

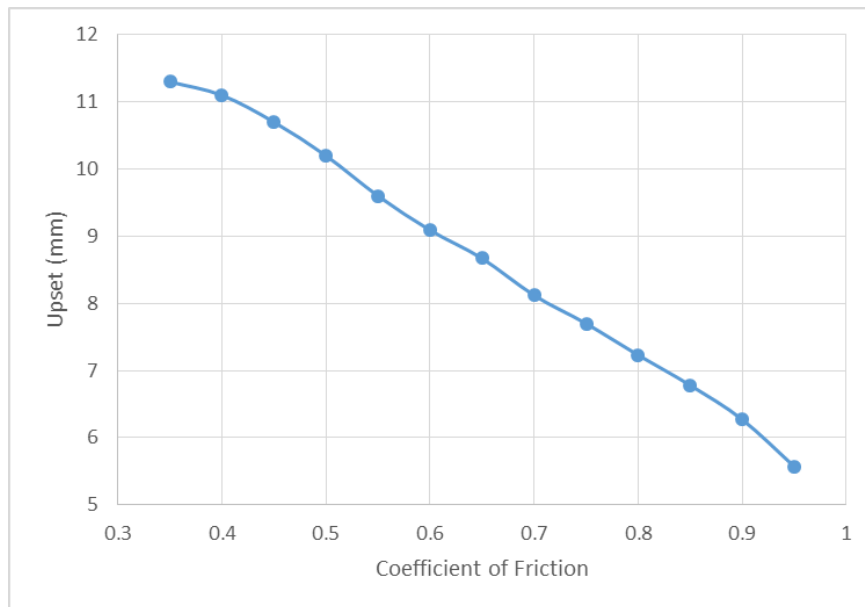


Figure 8: The effect of changing the coefficient of friction at the weld interface of model RFW1 on the FE upset value.

Table 5: New FE upset values obtained by modifying the coefficient of friction

Model no.	Actual upset (mm)	Co-eff. of friction before modification	FE upset before modification (mm)	Error in FE upset before modification (%)	Co-eff. of friction after modification	FE upset after modification (mm)	Error in FE upset after modification (%)
RFW2	3.65	0.7	5.26	44.1	0.95	3.86	5.8
RFW3	14.1	0.7	10.5	-25.5	0.49	13.6	-3.5
RFW4	4.39	0.7	5.24	19.4	0.85	4.56	3.9
RFW5	10.27	0.7	7.96	-22.5	0.53	9.9	-3.6
RFW6	14.63	0.7	10.5	-28.2	0.47	14.4	-1.6

3.2 FE Modelling of the FW process

The FE modelling of the process of screw press forging for each set of dissimilar tubes comprised four stages – (i) heating of the two tubes in a furnace, which lasted one hour; (ii) heat losses as the tubes were transferred in air to the press, which lasted 7 seconds; (iii) placing the tubes on the bottom die of the screw press until the top die started to move down, which lasted 5 seconds; and (iv) finally the processing of forging during which the top die moved down, pressing the tubes and joining them together. To prevent the tubes from sliding apart prior or during forging, they had been tack-welded together either by electron beam (performed in vacuum) or gas tungsten arc welding.

3.2.1 Generation of FE Model

The FE modelling was performed by employing the multi-operation simulation option in DEFORM. The material property data used in this simulation were the same as those derived and used in the reported RFW simulation. The diameter, length and wall thickness of the tubes for this simulation was found as 150 mm, 40 mm and 22 mm respectively. The top die had 19,868 elements, 20,304 nodes and a temperature of 250°C, and the bottom die had 19,869 elements, 20,302 nodes and a temperature of 230°C. Both dies were specified as being made of H13 tool steel and assigned rigid properties in the simulation. The tubes were assigned plastic properties. The 316L tube had 2,634 elements and 2,782 nodes; the S355 tube had 2,569 elements and 2,716 nodes. All the elements in the simulations were linear and the FE mesh for this forging model is shown in Figure 9.

There were four forging models developed in total, as can be seen in Figure 10. Models F1 and F2 had an initial temperature (in the furnace) of 1050°C, whereas models F3 and F4 had an initial temperature of 1100°C. Models F1 and F3 were pressed from an initial length of 80 mm to a final length of 60 mm, whereas models F2 and F4 were pressed to a final length of 50 mm. For all the models, the S355 tube was placed on the bottom die, with the 316L tube lying on top of it. The input parameters for the screw press forging machine were – (i) maximum machine energy of 160,000,000 N.mm, (ii) blow efficiency of 0.5, (iii) moment of inertia of 1,038,000 N.mm.s², (iv) lead screw pitch of 250 mm/rev. The numerical solver and re-meshing specifications were the same as those assigned in the RFW simulation. The step size in the forging model was kept constant at 0.0005 s/step in order to achieve numerical convergence. A slurry of graphite and water was used to lubricate the surfaces of the dies, and therefore a coefficient of friction of 0.3 was prescribed in the FE model at the contact surfaces between the tubes and the dies.

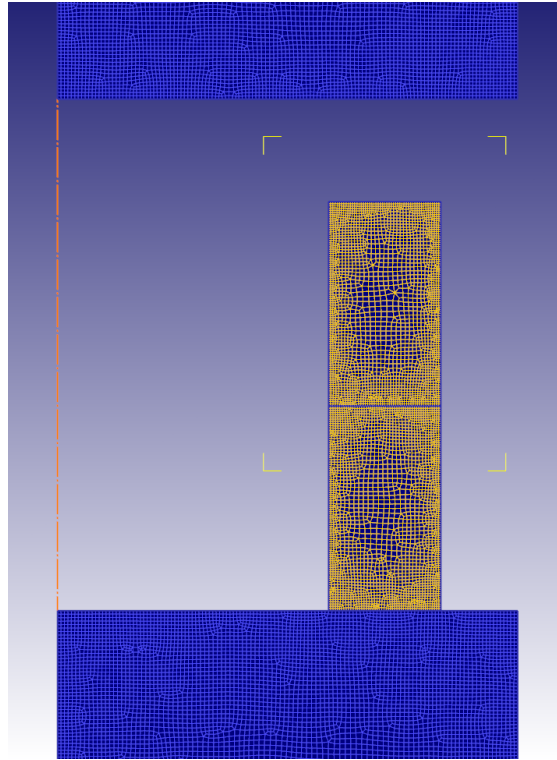


Figure 9: The FE mesh for the forging model

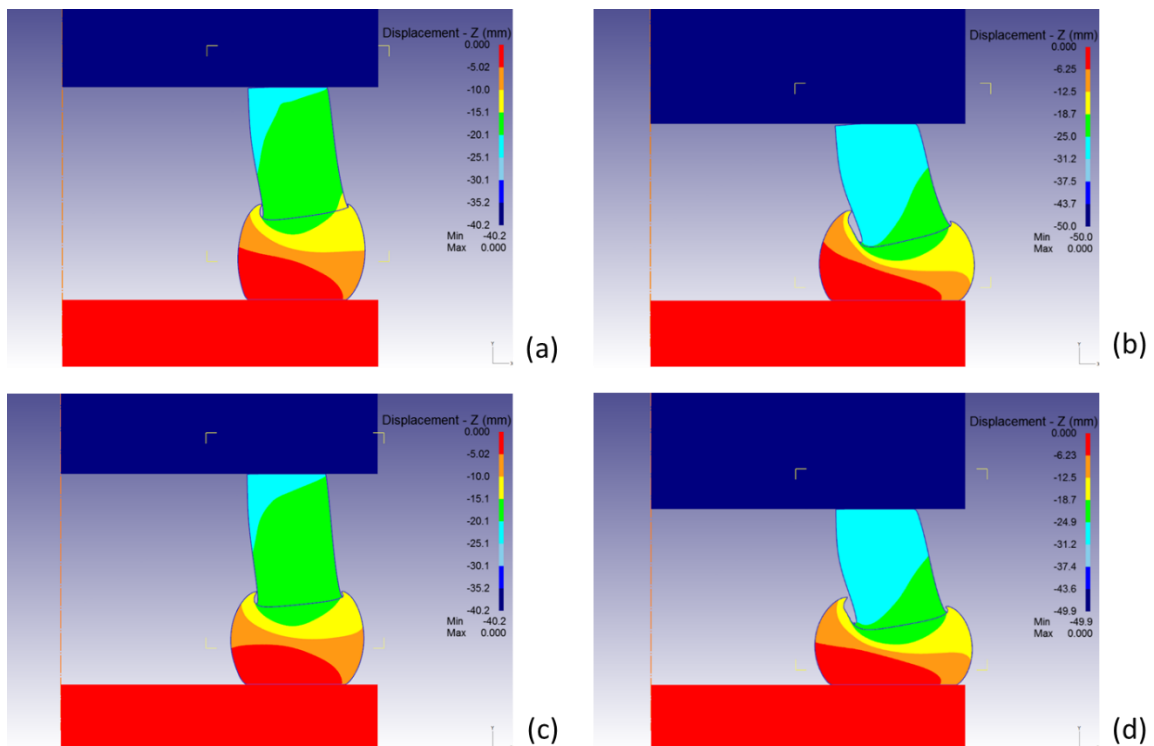


Figure 10: FE model (a) F1 (initial temperature of 1050°C and final height of 60 mm), (b) F2 (initial temperature of 1050°C and final height of 50 mm), (c) F3 (initial temperature of 1100°C and final height of 60 mm), and (d) F4 (initial temperature of 1100°C and final height of 50 mm) at the completion of forging

3.2.2 FE Results and Comparison with Experimental Measurements

The FE results, depicted in Figure 10, were compared to the experimental measurements (an image of actual forged ring is already shown in Figure 1) by considering the bulging of the tubes at the end of forging. Table 6 lists the maximum outer and minimum inner diameters of FE models compared to the experimental measurements at the completion of forging. It can be seen from the table that the difference between the FE and experimental diameters is between 0% and – 8.47%.

Table 6: Comparison between FE and experimental maximum outer and minimum inner diameters after forging.

Model No.	Experimental outer diameter (mm)	Experimental inner diameter (mm)	FE outer diameter (mm)	FE inner diameter (mm)	% difference between FE and experimental outer diameter	% difference between FE and experimental inner diameter
F1	175	103	173	100	-1.14	-2.91
F2	185	102.7	185	96.6	0	-5.94
F3	175	103	173	96	-1.14	-6.8
F4	185	102.7	185	94	0	-8.47

4. Experimental details

Figure 11 shows schematic of sample extraction scheme for tensile, microstructure and hardness tests from FW ring. Three ASTM standard tensile samples are extracted (120° apart from each other) from each of the ring in such a way that each sample contains half section of each of the two different steels and the weld line is at the centre of the gauge length. Similarly, two sections (180° apart from each other) have been extracted from the same ring and then EDM cut into rectangular sections for microstructure and hardness analysis. For each sample, the axis is always kept parallel to the forging axis of the ring during extraction and testing. The same sample extraction scheme has been followed for both RFW and EBW rings.

The tensile tests were performed in Zwick Z250 machine at room temperature. Each test was repeated three times for a particular ring in order to have a good statistical representation of the tensile properties and the values were averaged to obtain the average yield strength (YS) and ultimate tensile strength (UTS). The tests were performed at a strain rate of 0.01/s maintaining ASTM E8 standard [23]. The YS was calculated at a strain offset of 0.2% and the UTS was determined from the maximum stress value reached from each of the tests. Only tensile behaviour of selected rings (such as FW-02, FW-09, RFW-12 and EBW) are included in this study.

A Struers hardness tester was used for hardness measurement of one set of EDM cut rectangular sections according to ASTM standard E384 – 11 [24]. The indents were made in a rectangular matrix with a minimum of 40 indents at each side of the weld line using a Vickers indenter with a fixed load of 1kgf.

The distance between any two indents along both X and Y directions was kept as 1.5 mm and the indents altogether covered $\sim 0.2 - 4.5$ mm distance from both side of the weld line. It was not possible to accurately place indents exactly on the thin weld line of both FW and RFW rings, whereas an additional row of indents were placed on the thick weld line of the EBW ring to measure the hardness of the weld line. In this study, individual hardness distribution of FW-02, FW-09, RFW-12 and EBW rings as well as average hardness distribution of all FW and RFW rings are discussed.

Microstructural analysis was done on the other set of EDM cut rectangular sections. The samples extracted from FW-09, FEW-12 and EBW rings were mounted in the conductive resin moulds followed by grinding with SiC abrasive grit papers and polished using a UltraPol 9 μ m, Trident 3 μ m, MasterTex 1 μ m and Microcloth with 0.02 μ m colloidal silica suspension. The FW-09 and RFW-12 ring samples were then further vibro-polished with colloidal silica for EBSD analysis. The SEM images and EBSD data was collected using a FEI Quanta FEG 250 – SEM fitted with an Oxford instruments camera system and Aztec software operating with an accelerating voltage and working distance of 20kV and 20mm respectively. Orientation mapping was performed on a rectangular grid with a step size of 0.3 μ m and the indexing was $\sim 98\%$ for both samples. The corresponding data processing, including grain orientation, area fraction of grains and average misorientation, was then carried out using HKL Channel5 post processing software.

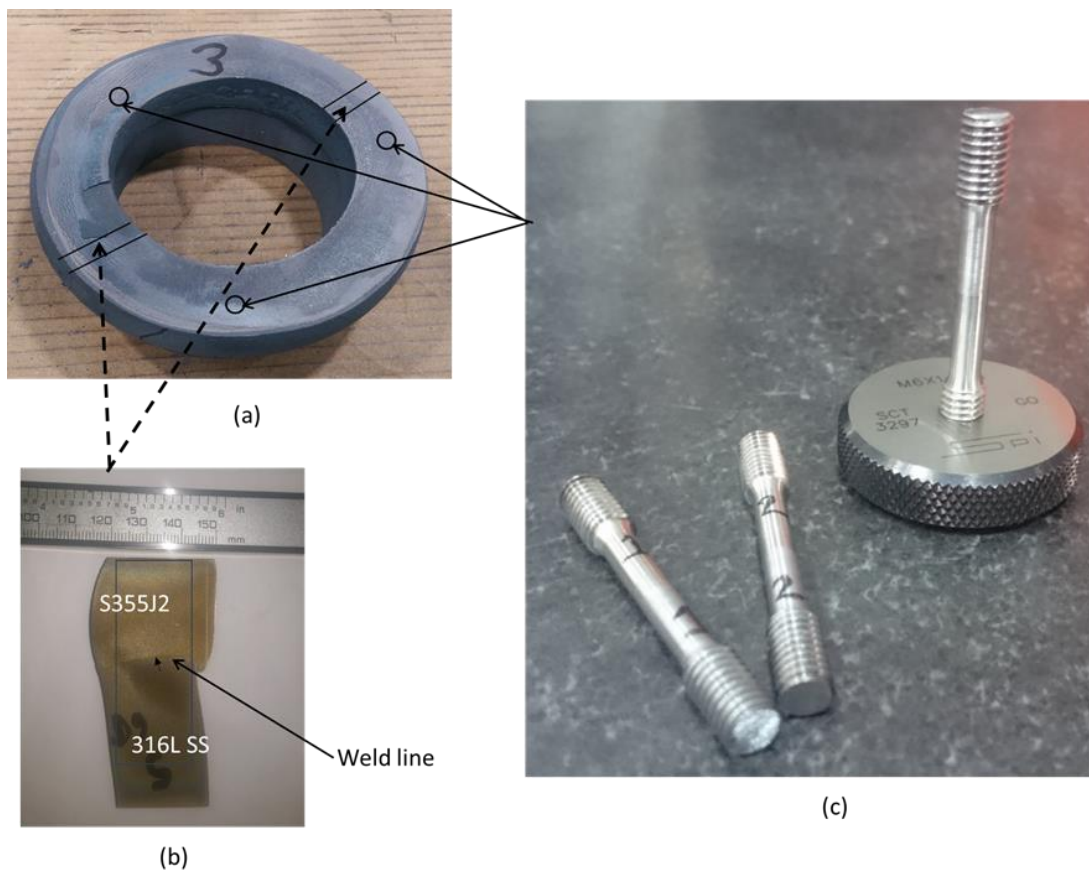


Figure 11: Schematic of sample extraction from FW ring – (a) forged ring marked for sample extraction positions, (b) rectangular sample extracted for microstructure and hardness analyses using wire EDM, (c) samples extracted for tensile testing. The same sample extraction scheme has been followed for RFW and EBW rings.

5. Results and discussion

5.1 Tensile properties

Figure 12 shows the tensile behaviour (3 repetitions per material condition) of selected FW-02, FW-09, RFW-12 and EBW rings. The true stress-strain curves for FW-02 and FW-09 rings (Figure 12a and Figure 12b) exhibited behaviour of a typical low carbon steel with clear indications of upper and lower yield points followed by strain hardening and necking prior to failure. The YS and UTS values of these two rings were observed in the range of ~320 – 360 MPa and ~640 – 670 MPa respectively. A more prominent strain hardening was seen for both RFW-12 and EBW rings (Figure 12c and Figure 12d), followed by an immediate necking particularly for EBW ring (Figure 12d). The YS and UTS values were observed slightly higher for RFW-12 ring (~270 MPa and ~670 MPa respectively) as compared to the EBW ring (~260 MPa and ~610 MPa respectively). Overall, these four rings showed similar UTS values, but considerably higher YS for both the FW rings. The strain to failure values of ~0.35, ~0.3 and ~0.1 for FW-09, RFW-12 and EBW rings respectively indicated the higher ductility for both FW-09 and RFW-12 rings as compared to the EBW ring. The FW and RFW samples showed gradual necking after strain hardening unlike the EBW ring. Figure 13 shows examples of the ductile failure of select tensile samples extracted from FW, RFW and EBW rings. It is important to note that the ductile failure occurred at either side of the dissimilar weld rather than at the weld zone for all cases indicating a sound joint. In most cases, failures occurred at S355J2 side due to its lower UTS and elongation properties as compared to the 316L side.

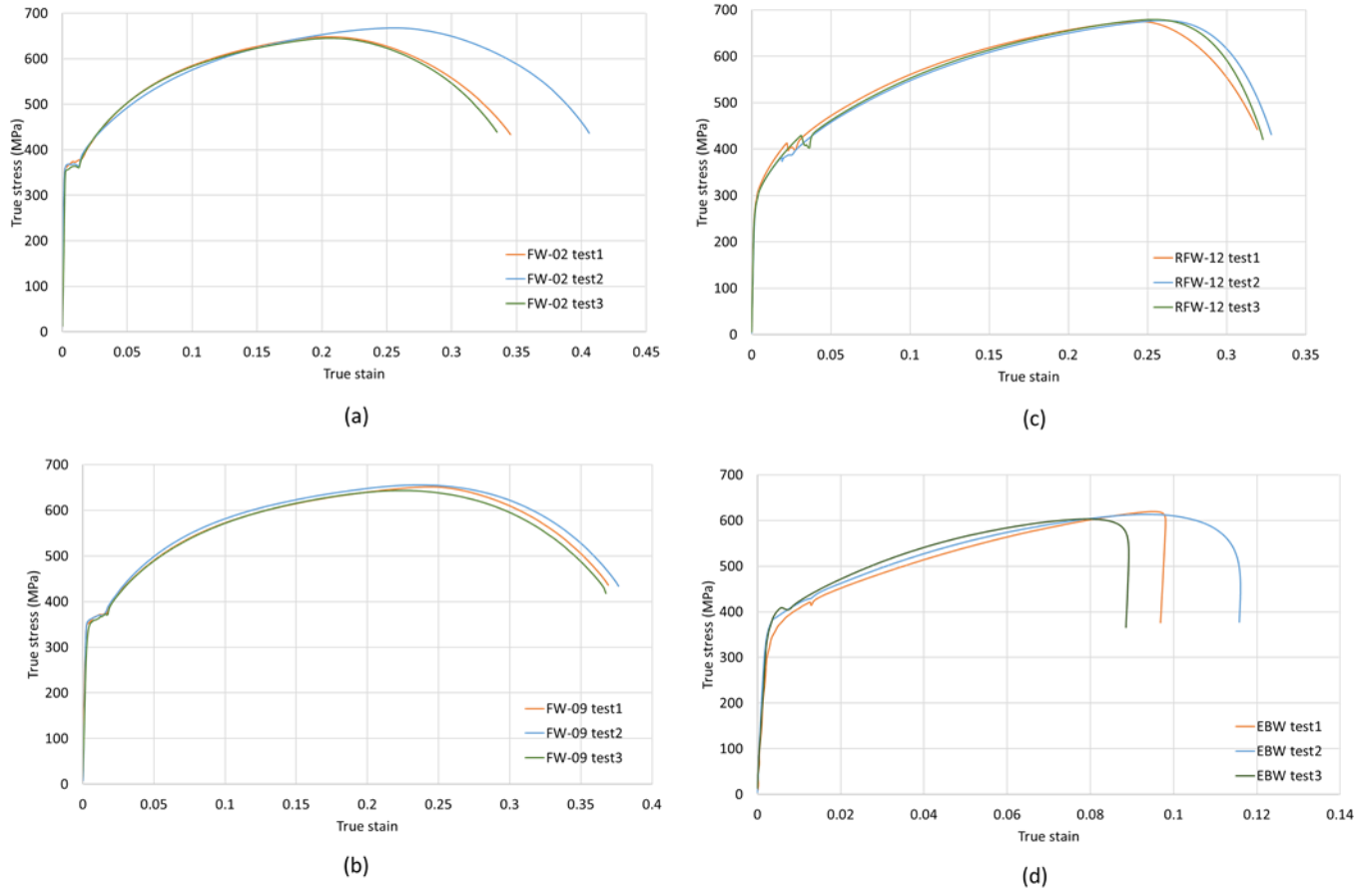


Figure 12: Tensile behaviour of selected (a) FW-02, (b) FW-09, (c) RFW-12 and (d) EBW rings

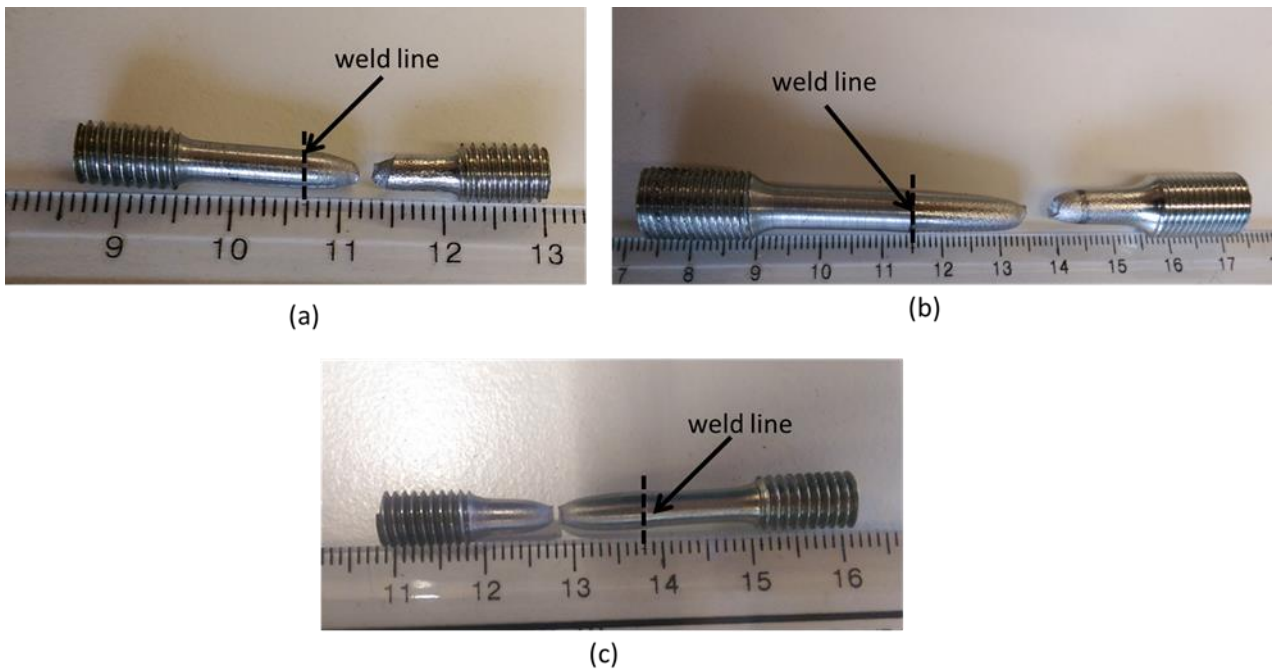


Figure 13: Failure of randomly selected tensile samples extracted from (a) FW, (b) RFW and (c) EBW rings

5.2 Hardness

Figure 14 shows the average hardness distribution of selected FW-02, FW-09, RFW-12 and EBW rings. The image of the weld zone with indent locations is provided at the left hand side of each hardness distribution map. Both FW-02 and FW-09 rings showed very uniform hardness distribution at both sides of the weld line with an average hardness value of ~167 HV and ~164 HV respectively (Figure 14a). The FW route had the advantage of temperature uniformity within the whole part during the operation and a relatively slow cool in air after forging eliminating any requirements for a PWHT. The RFW-12 ring showed relatively higher average hardness of ~187 HV with higher hardness in the S355J2 side of the weld line as compared to the other side (Figure 14b). The RFW process caused localised temperature rise of ~1000°C – 1400°C at the welding interface based on the type of steel and the variation in friction pressure [25], [26]. The large steel rings acted as heat sink causing the temperature to cool down very rapidly at the end of RFW operation, which had an effect of austenitizing followed by quenching on the S355J2 steel leading to its high hardness. The FW and the RFW process exposed both steels to high temperatures in excess of around 1000°C but the former resulted in much slower cooling of the part compared to the later. In case of the FW, the S355J2 side exhibited lower hardness compared to that in case of the RFW, where it exhibited comparatively higher hardness. This was due to the much faster cooling rate in RFW process resulting in higher amount of martensitic and some bainitic structure within and near the weld interface. During FW process, the cooling was much slower as compared to the RFW, so ferritic and pearlitic with some bainitic structure was very likely to form [27], [28].

The EBW ring showed a very high hardness of ~413 HV within the weld zone with considerable drop in hardness away from the weld zone, exhibiting ~206HV (Figure 14c). This is expected as localised melting was involved in EBW due to high energy density of the electron beam. Therefore, the EBW ring, depending on the service conditions, would require PWHT in most cases compared to the negligible requirement for PWHT in the solid-state joining routes. Despite the differences in hardness distribution in the three different manufacturing routes, it was noteworthy that the mechanical test samples for all these routes exhibited failure away from the weld line, as shown in mechanical testing section later.

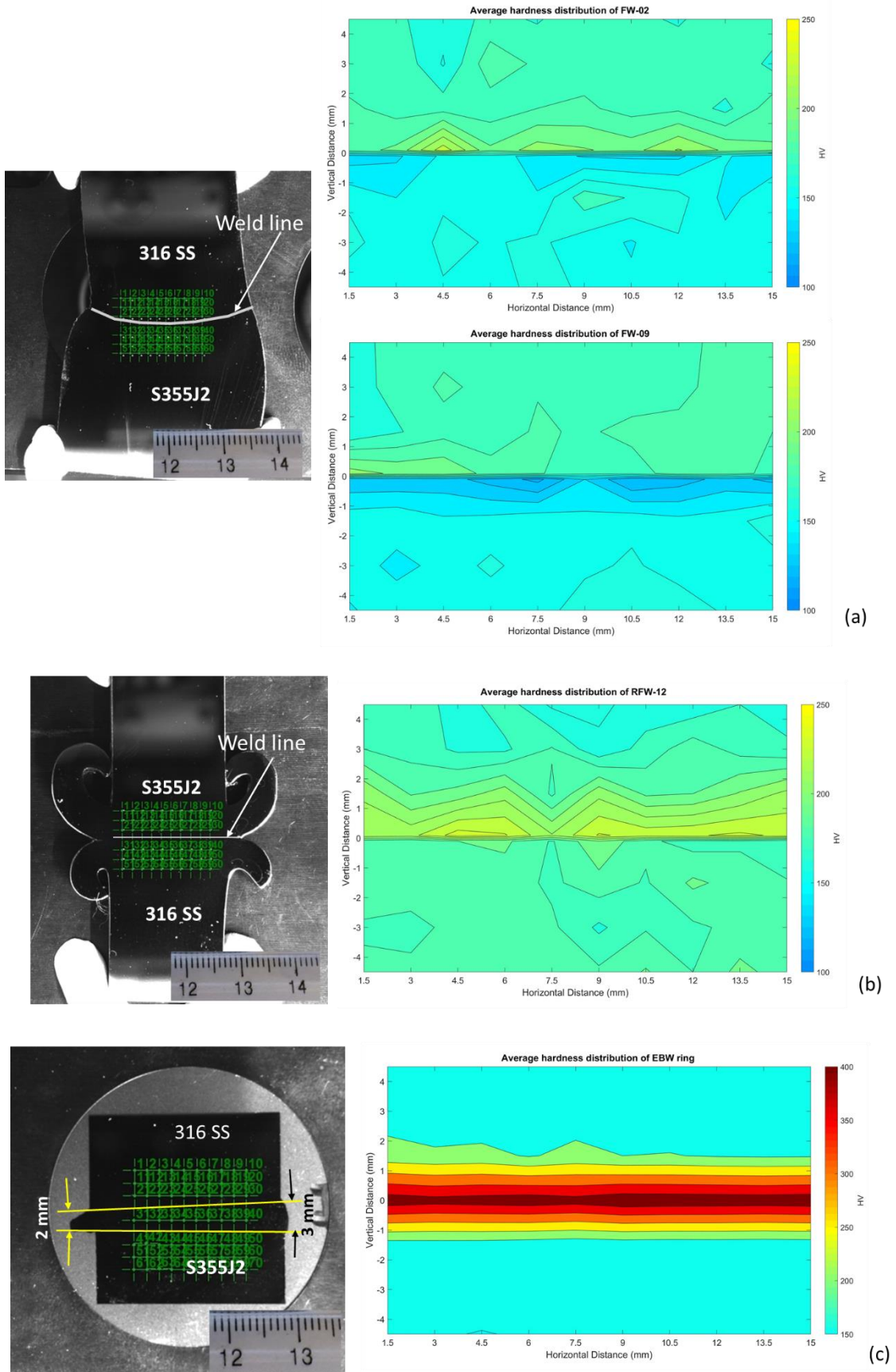


Figure 14: Average hardness distribution of selected (a) FW-02 and FW-09, (b) RFW-12 and (c) EBW rings

5.3 Microstructure

Figure 15 shows the microstructures of parent 316L SS and of S355J2 materials respectively, taken away from the weld interface. The 316L SS exhibits typical austenitic structure with annealing twins (Figure 15a) whereas the S355J2 exhibits mixture of ferritic and bainitic structure (Figure 15b). In a detailed investigation on S355J2 microstructure, a mixed ferritic and pearlitic structure was observed at room temperature, but cooling from high temperatures resulted in a mixture of ferritic and pearlitic and mixture of bainitic and martensitic microstructures depending on cooling rate [27]. In case of the FW process, the cooling rate was slow enough to produce a mixture of ferritic, pearlitic and possibly some bainitic structure. Figure 16a shows the microstructure of FW-09 ring around the weld zone, where equiaxed microstructure is observed in both parent S355J2 and 316L SS materials. The weld interface appears as a very thin line and the interface as such is free from any discontinuities and defects as seen in Figure 16b at higher magnification. The weld interface was found to be in the range of $\sim 1 - 5 \mu\text{m}$ wide, indicating almost no HAZ development due to the FW process. The FW microstructure was appeared very similar to a diffusion bonded microstructure for similar grades of steel [29], where the researchers investigated diffusion bonding of AISI 304 stainless steel and AISI 4140 medium carbon steel at temperature range of 750°C to 900°C and concluded that the bonds produced at 900°C exhibited highest shear strength. The diffusion like bond, in case of the FW process in current work, was produced instantly with a single blow of the screw press. The FW joint was inspected using ultrasound and did not exhibit any defects.

Figure 17a shows the microstructure of RFW-12 part around the weld zone exhibiting acicular structure within the weld interface and on the S355J2 side and equiaxed austenitic structure on the 316LSS side. The localized heating to $\sim 1100^\circ\text{C}$ followed by rapid cooling occurring in the RFW led to acicular microstructure (consisting of mixture of martensite and bainite) and increased average hardness (Figure 14b) particularly on the S355J2 side of the weld. The weld interface in this case was slightly thicker, $\sim 20 - 30 \mu\text{m}$, compared to the FW case and exhibited acicular structure (Figure 17b). Figure 18 shows lower magnification montage of four SEM images taken to the left side region of the Figure 17a, extending into S355J2 side, revealing distinct TMAZ and HAZ zones present between the weld interface and the parent on the S355J2 side of the weld. The TMAZ exhibited acicular structure similar to that within the weld interface and extended to about 1.5 mm from the weld interface and the HAZ exhibited a markedly refined grain structure extending 0.5 mm further from the edge of the TMAZ toward the larger grain equiaxed structure of S355J2 parent.

Figure 19a shows microstructure of the EBW part around the weld zone. A homogenous columnar dendritic microstructure was observed within the $\sim 2 - 3 \text{ mm}$ thick weld zone. A prominent HAZ (~ 1.5

mm wide) was observed extending from the edge of the weld zone, on the S355J2 side, towards the equiaxed grain structure of the S355J2 parent. The HAZ contained a mixture of martensitic (in the immediate vicinity of the weld zone) and markedly refined equiaxed grain structure (extending towards larger grain equiaxed structure of S355J2 parent). This could be attributed to cooling rate being maximum within the weld zone and reducing gradually away from it caused formation of acicular structure in the immediate vicinity of the weld zone and more refined grain structure slightly away from the same. The 316L side of the weld zone, on the other hand, exhibited equiaxed austenitic grain structure without showing any presence of a HAZ. It was reported for dissimilar steel welds that the weld microstructure was predominantly equiaxed for austenitic and duplex steels but columnar for ferritic steels [30]. On the other hand, formation of dendritic weld microstructure was reported for dissimilar metal welds, such as Inconel 625 and stainless steel 304L, due to their differences in thermal conductivity [31]. In this study, the formation of columnar dendritic weld microstructure was attributed to the significantly different thermal conductivity of both S355J2 and 316L ($\sim 40 - 45$ W/m-K [32] and $\sim 13 - 17$ W/m-K [33] respectively), which in turn led to significantly higher hardness at the weld zone (Figure 14c) compared to both parent materials zones. Figure 19b – d show magnified SEM images of S355J2 side of the weld, centre of the weld zone and 316L side of the weld respectively. A small amount of very fine pores were observed in the welds irrespective of the processing routes (as in Figure 16a, Figure 17b and Figure 19a), but it did not influence the weld strength in any of the cases as demonstrated from the tensile test results of the different welds.

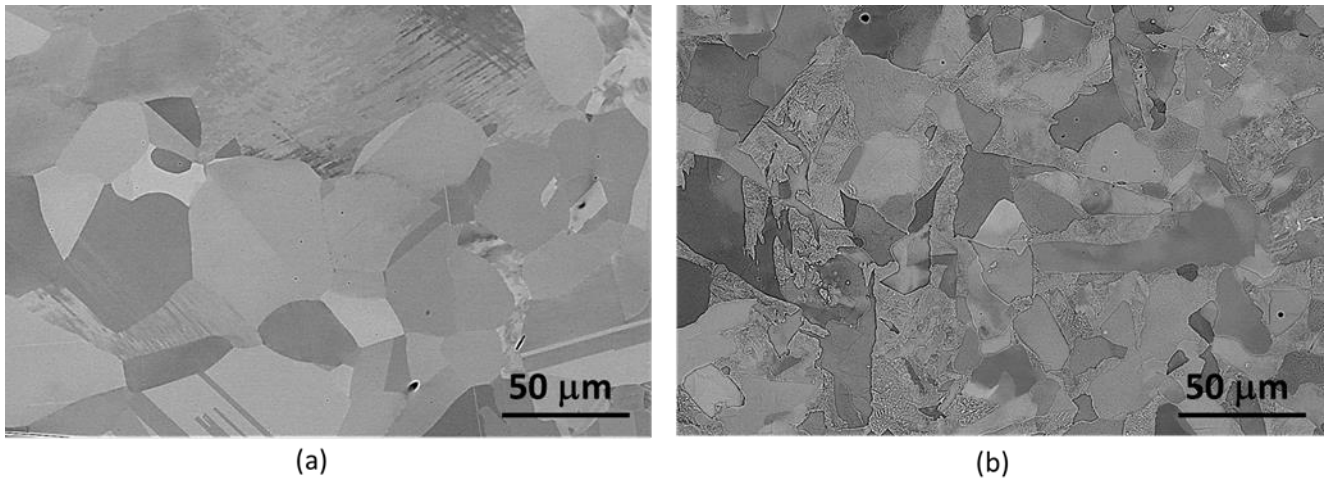


Figure 15: Microstructures of parent (a) 316L SS and (b) S355J2 materials

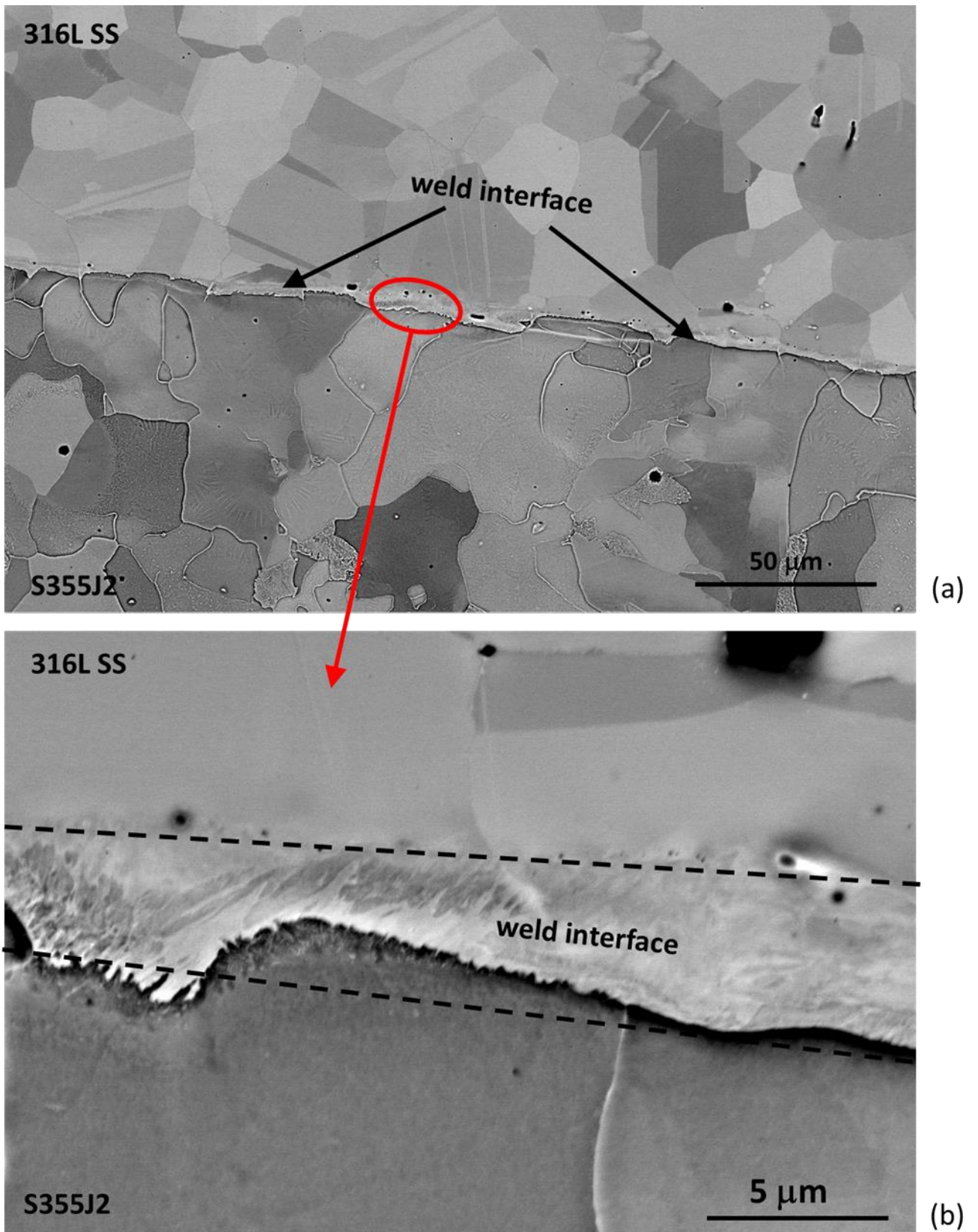


Figure 16: (a) Microstructure of FW-09 ring around the weld zone and (b) high resolution image of the thin FW weld interface

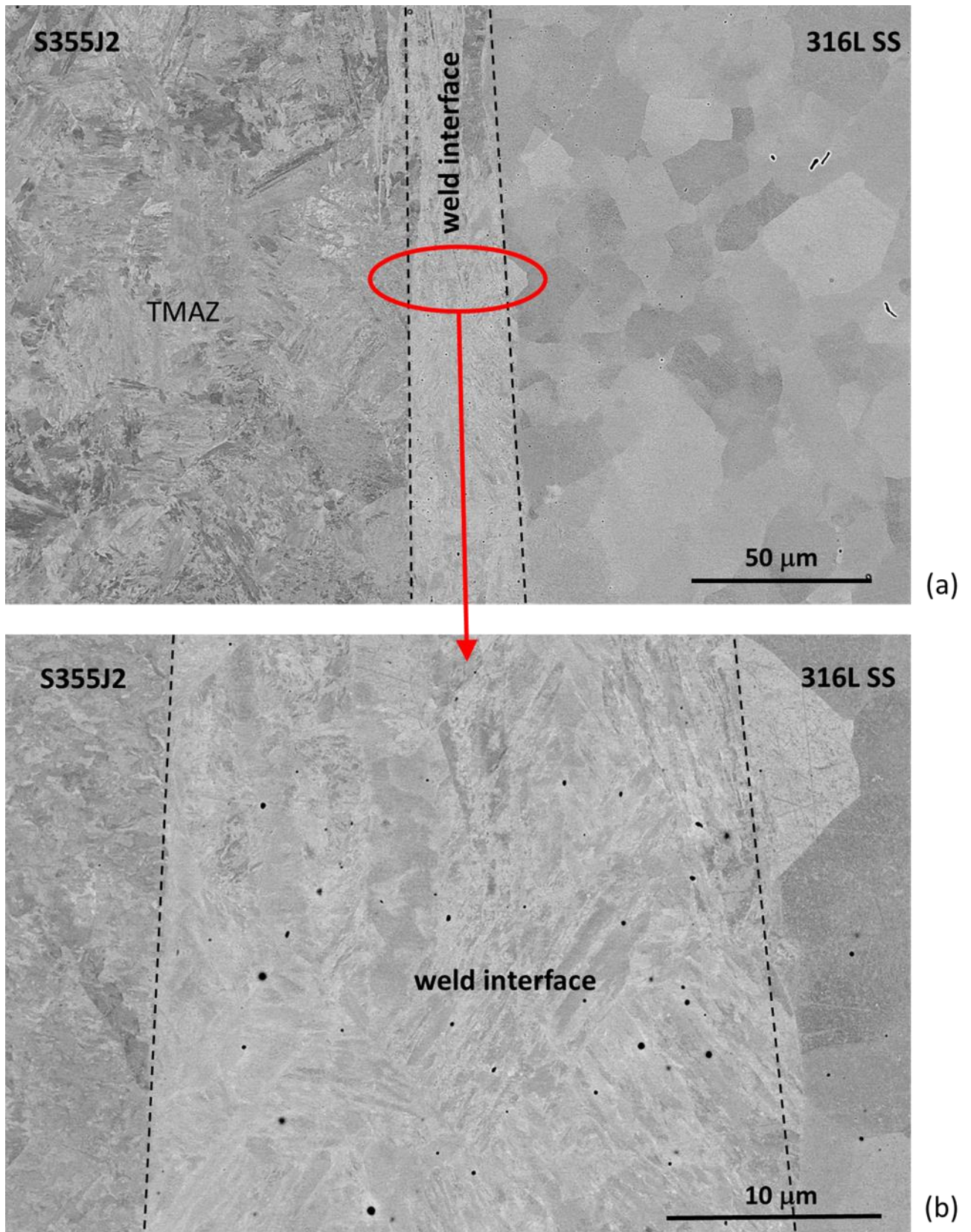


Figure 17: (a) Microstructure of RFW-12 ring around the weld zone and (b) high resolution image of the RFW weld interface

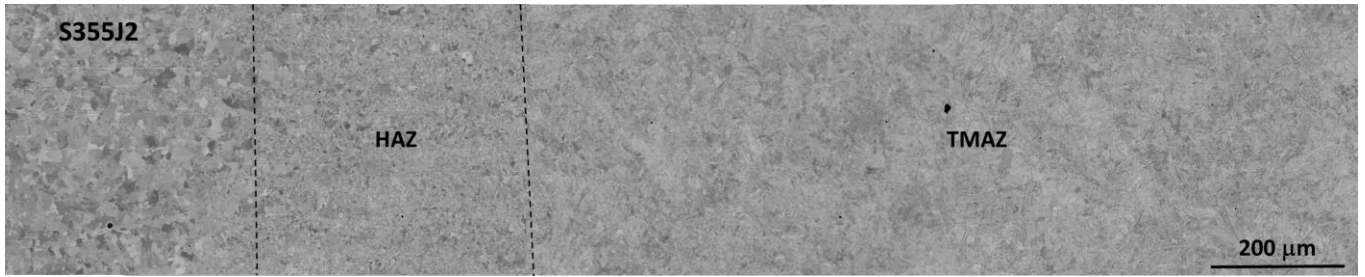


Figure 18: Microstructure of the TMAZ and HAZ at the S355J2 side for the RFW weld

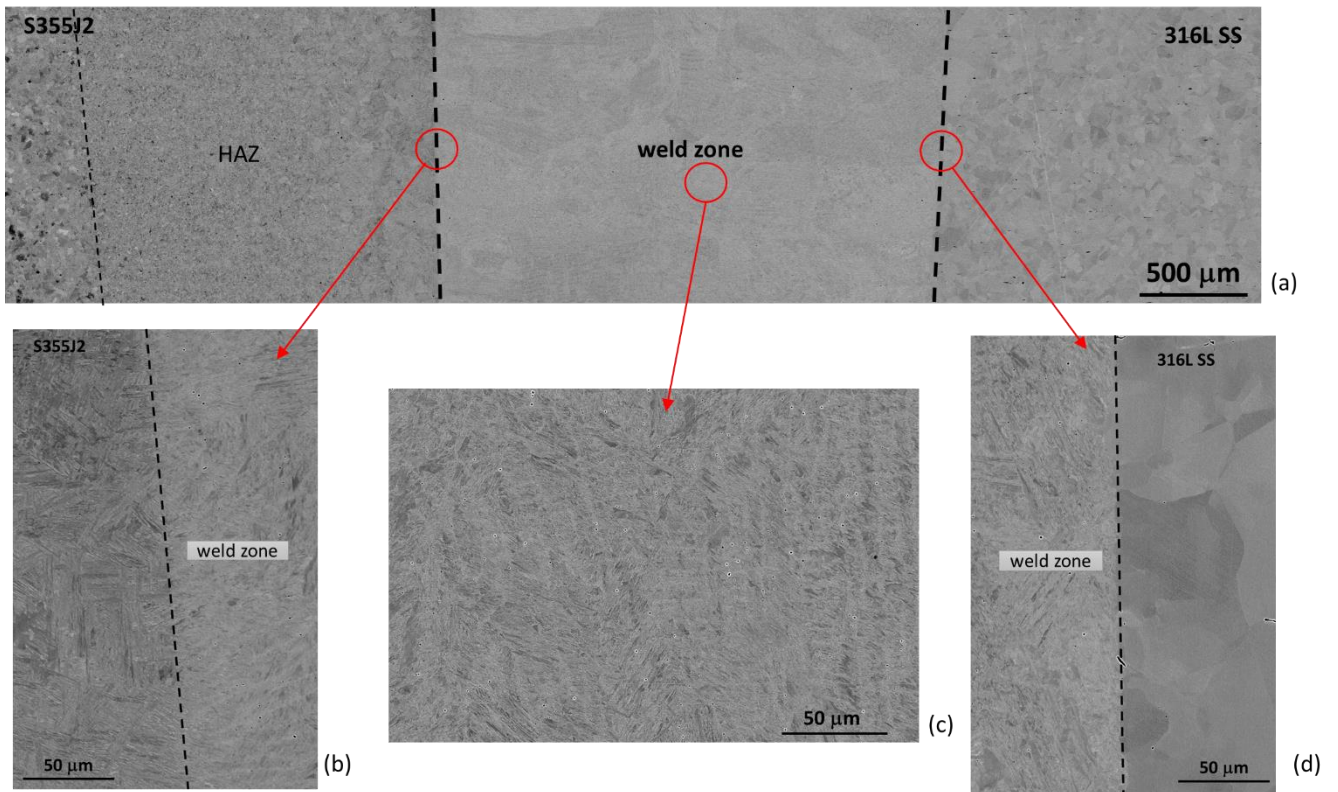


Figure 19: Microstructure of EBW ring – (a) low magnification image around the weld zone, (b) microstructure of the weld zone at the S355J2 side, (c) microstructure at the centre of the EBW weld zone, and (d) microstructure of the weld zone at the 316L SS side

To further complement and compare the microstructure investigation of the FW and the RFW samples, EBSD analysis was carried out on FW-09 and RFW-12 specimens. Figure 20 summarises the EBSD analysis of FW-09 ring at the weld zone. The forging direction and the radial direction of the ring are denoted as ND and RD respectively. Figure 20a shows the band contrast (BC) image of the FW ring, where a very thin weld line is noticeable. Figure 20b shows the phase map, where both S355J2 steel and 316L are identified by BCC (yellow) and FCC (blue) crystal structures respectively. The very thin weld line has not been properly indexed, thus it appears as white. Figure 20c shows the inverse pole figure (IPF) map, where random orientation of grains is observed for both parent materials. The recrystallization map is shown in Figure 20d, where recrystallized, sub-structured and deformed grains are shown in blue, yellow and red colours respectively. Both parents showed mostly recrystallized

(defined by misorientation angle $\geq 15^\circ$) and sub-structured (defined by misorientation angle $\sim 5^\circ - 15^\circ$) grains, but almost no deformed (defined by misorientation angle $\leq 5^\circ$) grains. The amount of recrystallized grains was found $\sim 39\%$ and $\sim 55\%$ for S355J2 steel and 316L respectively, whereas the rest was the sub-structured grains. The dominant mechanism during high strain rate hot deformation of 316LN stainless steel is dynamic recovery to some extent followed by static recrystallization during cooling after forging [34], [35]. At high strain rates of 10 s^{-1} , which is similar to the strain rates of the screw press forging employed in the current work, the dominant mechanisms for softening of medium carbon steel are static recrystallization and dynamic recovery [29]. This is substantiated by the observations from the current work where the EBSD analysis in Figure 20d shows that most of the microstructure of the 316L and the S355J2 is occupied by recrystallized and sub-structured zones. Figure 20e shows the Kernel Average Misorientation (KAM) map indicating the strain distribution at the weld zone. The scale bar shows the highest and lowest levels of misorientations by red and blue colours respectively within the scanned area. The level of misorientation was found lowest (indicated by mainly blue) in S355J2 steel parent and slightly higher (indicated by both blue and green) in 316L SS parent due to complete absence of HAZ. The FW ring experienced a slower cool down after forging, due to air cooling, leading to very low residual strain throughout the part, which in turn showed low levels of misorientation. Overall the EBSD analysis of the FW ring showed the remarkable characteristics of this joining technique which did not appear, at all, to affect the parent material areas even in the very close vicinity of the weld line. The FW process produces an instant diffusion like bond with added benefit of the whole component being annealed as a result of forging and air cooling promoting homogenous microstructure and uniform mechanical properties.

Similarly, Figure 21 summarises the EBSD analysis of RFW-12 ring at the weld zone. The welding direction and the radial direction of the ring are denoted as ND and RD respectively. Figure 21a shows the band contrast (BC) image of the RFW ring, where a comparatively thicker weld line joined both parent materials. The weld line is marked by two dotted white lines. The rapid localized cooling of the HAZ resulted in acicular microstructure in the S355J2 side, whereas the 316L SS side retained its austenitic structure. Thus, RFW showed very dissimilar grain size in both parent materials at the weld zone unlike the FW case. Figure 21b shows the phase map, where both S355J2 steel and 316L SS parents are identified by BCC (blue) and FCC (yellow) crystal structures respectively. The weld line, marked by two dotted black lines, showed BCC (blue) crystal structure similar to S355J2 steel parent. The inverse pole figure (IPF) map is shown in Figure 21c. S355J2 steel and 316L SS parents contained grains mostly oriented at 101 and 001 directions respectively, whereas the weld line consisted of randomly oriented grains. Figure 21d shows recrystallization map, where recrystallized, sub-structured and deformed grains are shown in blue, yellow and red colours respectively. Due to development of HAZ, both parent materials and the weld line showed mostly deformed (defined by misorientation angle

$\leq 5^\circ$) and sub-structured (defined by misorientation angle $\sim 5^\circ - 15^\circ$) grains, but very few recrystallized (defined by misorientation angle $\geq 15^\circ$) grains. The amount of deformed grains was observed $\sim 79\%$, $\sim 33\%$ and $\sim 87\%$ for S355J2 steel parent, 316L SS parent and the weld line respectively. The amount of recrystallized grains was found in the range of 4 – 10%, whereas the rest is the sub-structured grains. Figure 21e shows the Kernel Average Misorientation (KAM) map indicating the strain distribution at the weld zone. The scale bar at the bottom shows the highest and lowest levels of misorientations by red and blue colours respectively within the scanned area. The formation of HAZ during RFW led to increase in the level of misorientation (indicated by mainly green and slightly blue) in both the parent materials as well as in the weld line. The RFW process involved rapid heating of the localised regions at the interface and the instant forging impact followed by very rapid cooling generated a level of residual strain, which was evident from the higher levels of misorientation observed at the weld zone. It should be noted that the level of misorientation was clearly higher in RFW process (Figure 21e) as compared to FW process (Figure 20e).

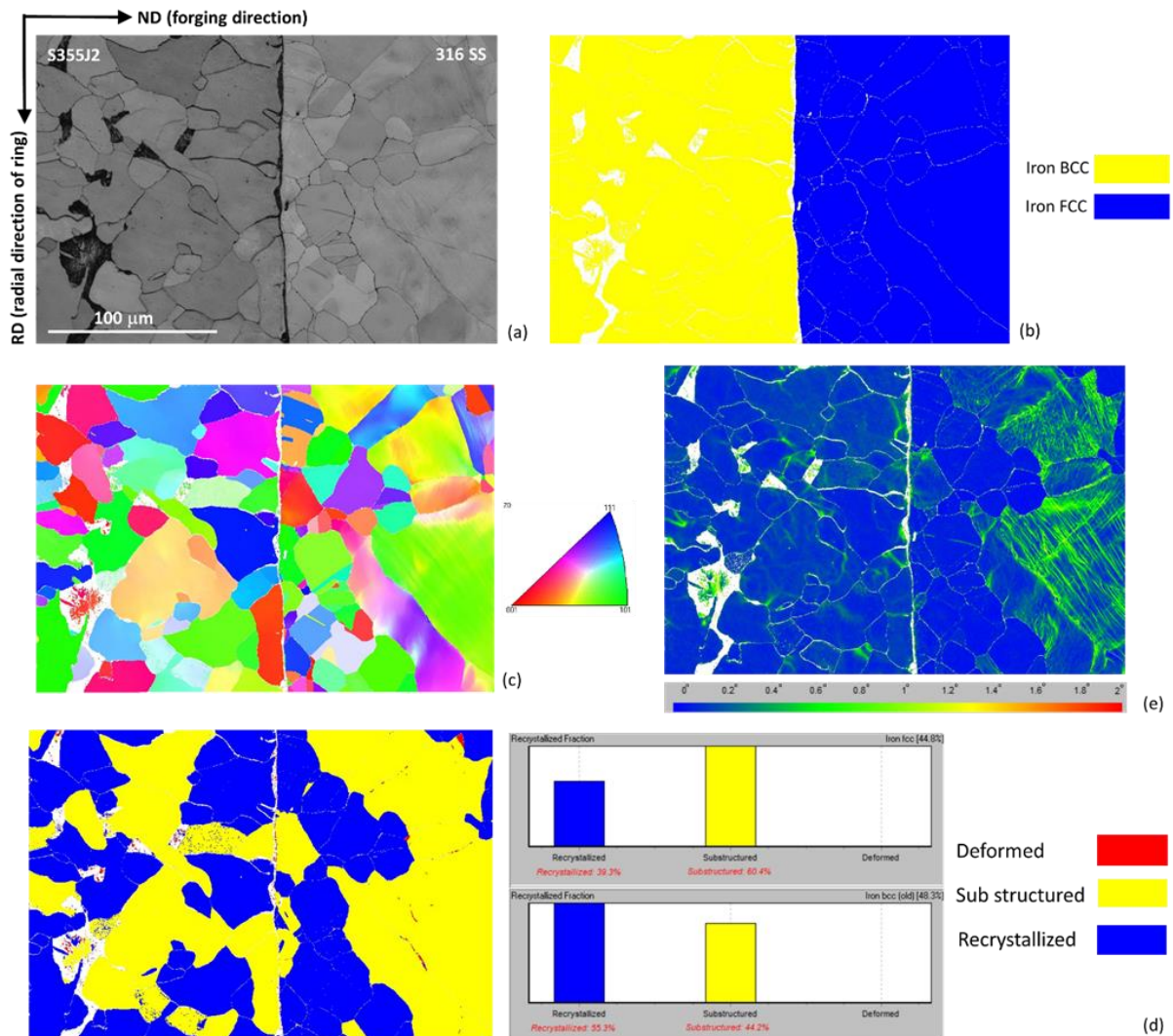


Figure 20: EBSD analysis of FW-09 ring at weld zone – (a) band contrast (BC) image, (b) phase map, (c) IPF map, (d) recrystallization map and (e) KAM map. The white areas in all images indicate the areas with no indexing.

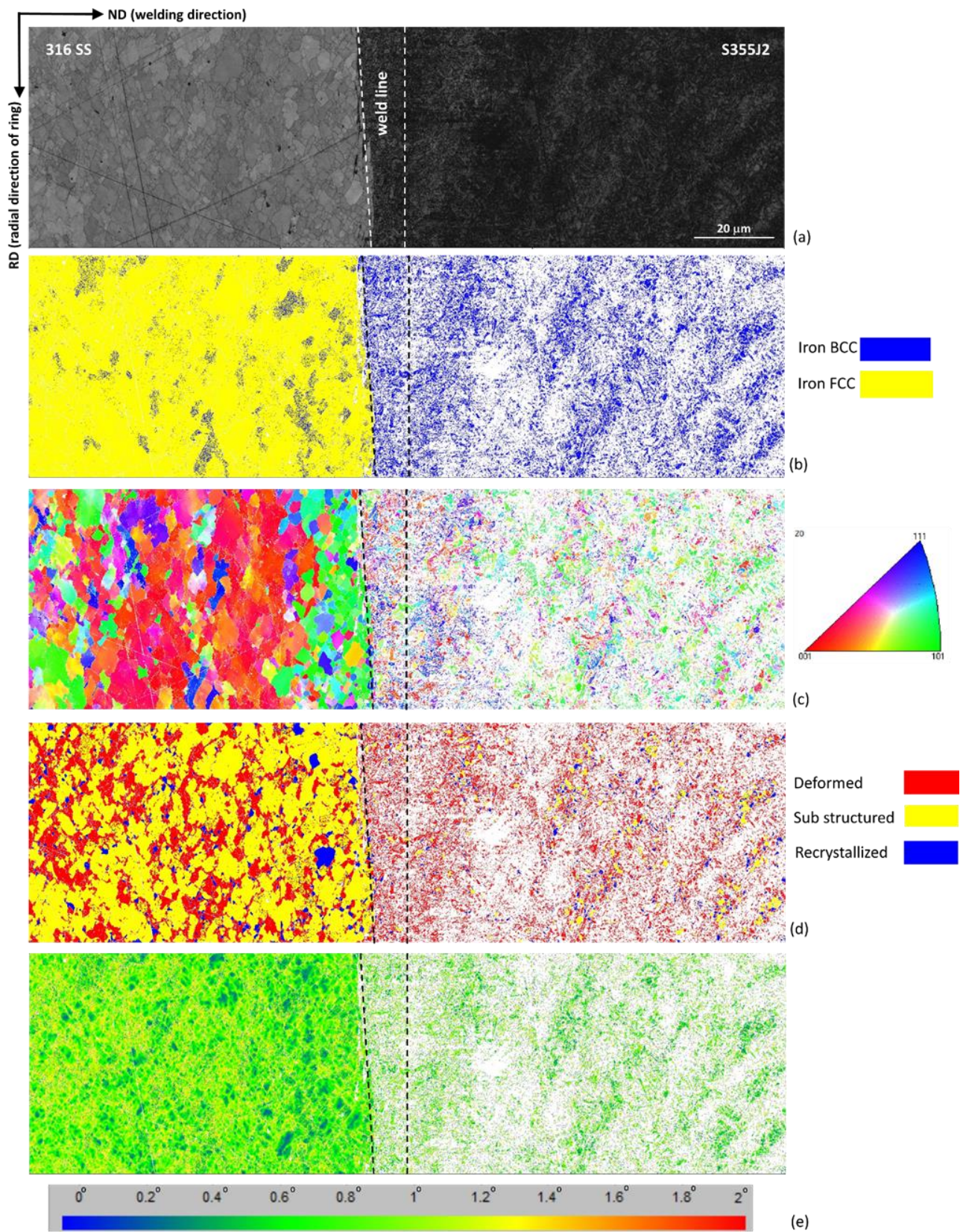


Figure 21: EBSD analysis of RFW-12 ring at weld zone – (a) band contrast (BC) image, (b) phase map, (c) IPF map, (d) recrystallization map and (e) KAM map. The white areas in all images indicate the areas with no indexing.

The three different manufacturing routes employed in the current work have been demonstrated to be effective in manufacture of the transition hybrid coupling demonstrator from dissimilar steels. The two solid-state routes result in very homogeneous properties across the weld eliminating requirements for PWHT whereas the EBW process results in a sharp gradient in hardness distribution across the weld suggesting further requirement for a suitable PWHT before an end application. Comparatively the solid-state process routes are simpler than the EBW route in that the later requires careful optimization of weld parameters to produce welds without defects. A 2100T Schuler screw press was employed for the FW process in this work and it was noted that as low as 50% press energy (Table 2) was adequate in producing a sound forge weld for the preform size of 150 mm OD. Hence, a larger coupling can also be manufactured on the 2100T press requiring appropriate sized die set by utilising up to 95% press energy. Similarly, there are screw presses available in forging industries, which exceed 32000T capacity, and therefore providing a viable option for manufacturing very large hybrid couplings, possibly exceeding well over 500 mm OD if required. The RFW process in this work was carried out on 125T capacity machine. There are machines of capacity up to 2000T available, however due to the size limitations on maximum diameter the machine can accommodate, maximum ODs possible ought to be in the range of 500 mm. On the other hand, the weld produced using the standard EBW process required a suitable annealing treatment to homogenize the significant difference between the parent and the weld hardness. Moreover the size limitations on the EBW machine and ability to accommodate a large preform in vacuum chamber would restrict maximum diameter that preforms could be welded to below 500 mm.

6. Conclusions

The following conclusions are drawn from this study:

- The FW process produced an instant diffusion-like bond at the weld interface between the two different steels with very uniform mechanical properties and absence of any HAZ on either side of the weld interface owing to the solid-state nature of the process and lack of any severe deformation mechanisms involved.
- The RFW process produced a weld interface with distinguishable TMAZ and HAZ regions containing acicular and refined equiaxed microstructure, respectively, on the S355J2 side of the weld owing to rapid cooling of the weld occurring in the RFW process whereas the 316L side exhibited equiaxed austenitic structure without any apparent TMAZ or HAZ. Despite differences in microstructure characteristics across the weld, hardness variation was not significant.
- The EBW process resulted in a 2-3 mm wide weld interface with distinct HAZ on the S355J2 side of the weld containing acicular structure in the immediate vicinity of the weld and very refined equiaxed structure towards larger grain equiaxed structure of the S355J2 parent. The 316L side of

the weld exhibited equiaxed austenitic structure with no apparent HAZ. The hardness distribution had significant gradient between the weld (3 times higher) and the parent. Although an effective process for producing hybrid transition coupling, the EBW dissimilar joint will require a tailored post-weld heat treatment to homogenize microstructure and mechanical properties across the weld.

- In FE analysis, the outcome of a parametric study proved that modifying the coefficient of friction prescribed during the modelling of RFW brought the maximum error of predicting the upset from 44.1% to 5.8%. The error of numerically predicting the change in the outer and inner tube diameter due to FW is within 1.14% and 8.47% respectively.
- The FW and the RFW processes offer an effective and simpler alternative solution to producing safe-end transition joints using conventional arc-welding techniques requiring complex multilayer weldments produced from a wide range of carefully selected fillers. Large scale and high integrity hybrid transition couplings can be produced with these solid-state processes without requiring any post-weld heat treatments.

Acknowledgement

The authors would like to acknowledge High Value Manufacturing Catapult for funding this work from their Innovate UK core grant (2013-2018, grant number-160051).

Author contribution

Himanshu Lalvani conceptualised, scoped and secured funding for the project. He led the project and managed the mechanical and microstructural experiments, data collection and analysis. Anas Yaghi led the finite element process modelling of FW and RFW processes as well as contributed in RFW process optimisation at MTC. Pedro Santos carried out the RFW trials at MTC. Bernd Baufeld led the manufacture of GTAW and EBW seal welded preforms and manufacture of through thickness EBW part at NAMRC. Paranjayee Mandal was involved in the data analysis of experimental outputs and wrote the manuscript draft. All authors read and approved the final manuscript.

References

- [1] Hänninen H, Aaltonen P, Brederholm A, Ehrnsteñ U, Gripenberg H, Toivonen A, et al. Dissimilar metal weld joints and their performance in nuclear power plant and oil refinery conditions. VTT Tied - Valt Tek Tutkimusk 2006:3–208.
- [2] Dak G, Pandey C. A critical review on dissimilar welds joint between martensitic and austenitic steel for power plant application. *J Manuf Process* 2020;58:377–406. <https://doi.org/10.1016/j.jmapro.2020.08.019>.
- [3] Lundin CD. Dissimilar Metal Welds-Transition Joints Literature Review Emphasis is on carbon migration, the stress/strain state of welds, and transition joint failure mechanisms. *Weld Res Suppl* 1982:58s-63s.

- [4] Kumar Singh D, Sahoo G, Basu R, Sharma V, Mohtadi-Bonab MA. Investigation on the microstructure—mechanical property correlation in dissimilar steel welds of stainless steel SS 304 and medium carbon steel EN 8. *J Manuf Process* 2018;36:281–92. <https://doi.org/10.1016/j.jmapro.2018.10.018>.
- [5] Satyanarayana V V., Reddy GM, Mohandas T. Dissimilar metal friction welding of austenitic-ferritic stainless steels. *J Mater Process Technol* 2005;160:128–37. <https://doi.org/10.1016/j.jmatprotec.2004.05.017>.
- [6] Sunay TY, Sahin M, Altintas S. The effects of casting and forging processes on joint properties in friction-welded AISI 1050 and AISI 304 steels. *Int J Adv Manuf Technol* 2009;44:68–79. <https://doi.org/10.1007/s00170-008-1810-0>.
- [7] Butrim VN, Beresnev AG, Denisov VN, Klyatskin AS. Experience in HIP Diffusion Welding of Dissimilar Metals and Alloys. *Hot Isostatic Press HIP'17* 2019;10:65–72. <https://doi.org/10.21741/9781644900031-9>.
- [8] Zuback JS, Palmer TA, DebRoy T. Additive manufacturing of functionally graded transition joints between ferritic and austenitic alloys. *J Alloys Compd* 2019;770:995–1003. <https://doi.org/10.1016/j.jallcom.2018.08.197>.
- [9] Punshon C, Ferhati A, Uk C, Dear M, Field A, Uk H. Dissimilar metal joining for pressure plant and forge tools n.d.:1–6.
- [10] Baufeld B, Priest J, Dutilleul T. EBW of nuclear pressure vessel steels. *Electrotech Electron* 2019;53:5–6.
- [11] OVAKO. Steel grade 2017:6–8.
- [12] T. F. Kong, L. C. Chan, T. C. Lee. Experimental Study of Effects of Process Parameters in Forge-Welding Bimetallic Materials: AISI 316L Stainless Steel and 6063 Aluminium Alloy. *Strain* 2009. <https://doi.org/10.1111/j.1475-1305.2008.00445.x>.
- [13] Węglowski MS, Błacha S, Phillips A. Electron beam welding - Techniques and trends - Review. *Vacuum* 2016;130:72–92. <https://doi.org/10.1016/j.vacuum.2016.05.004>.
- [14] Sun Z, Karppi R. The application of electron beam welding for the joining of dissimilar metals: An overview. *J Mater Process Technol* 1996;59:257–67. [https://doi.org/10.1016/0924-0136\(95\)02150-7](https://doi.org/10.1016/0924-0136(95)02150-7).
- [15] Desu RK, Nitin Krishnamurthy H, Balu A, Gupta AK, Singh SK. Mechanical properties of Austenitic Stainless Steel 304L and 316L at elevated temperatures. *J Mater Res Technol* 2016;5:13–20. <https://doi.org/10.1016/j.jmrt.2015.04.001>.
- [16] Blandford RK, Morton DK, Snow SD, Rahl TE. Tensile stress-strain results for 304L and 316L stainless steel plate at temperature. *Am Soc Mech Eng Press Vessel Pip Div PVP* 2008;6:617–28. <https://doi.org/10.1115/PVP2007-26096>.
- [17] Mäkeläinen P, Outinen J, Kesti J. Fire design model for structural steel S420M based upon transient-state tensile test results. *J Constr Steel Res* 1998;48:47–57. [https://doi.org/10.1016/S0143-974X\(98\)00005-4](https://doi.org/10.1016/S0143-974X(98)00005-4).
- [18] Yaghi AH, Hyde TH, Becker AA, Sun W. Finite element simulation of residual stresses induced by the dissimilar welding of a P92 steel pipe with weld metal IN625. *Int J Press Vessel Pip* 2013;111–112:173–86. <https://doi.org/10.1016/j.ijpvp.2013.07.002>.
- [19] Yaghi AH, Hyde TH, Becker AA, Williams JA, Sun W. Residual stress simulation in welded sections of P91 pipes. *J Mater Process Technol* 2005;167:480–7. <https://doi.org/10.1016/j.jmatprotec.2005.05.036>.
- [20] Parthasarathi NL, Borah U, Albert SK. Correlation between coefficient of friction and surface

- roughness in dry sliding wear of AISI 316 L (N) stainless steel at elevated temperatures. *Comput Model New Technol* 2013;17:51–63.
- [21] Villa M. Metallurgical and mechanical modelling of Ti-6Al-4V for welding applications. Thesis 2016.
- [22] D’Alvise L, Massoni E, Walloe SJ. Finite element modelling of the inertia friction welding process between dissimilar materials. *J Mater Process Technol* 2002;125–126:387–91. [https://doi.org/10.1016/S0924-0136\(02\)00349-7](https://doi.org/10.1016/S0924-0136(02)00349-7).
- [23] ASTM E8. ASTM E8/E8M standard test methods for tension testing of metallic materials 1. *Annu B ASTM Stand* 4 2010:1–27. <https://doi.org/10.1520/E0008>.
- [24] ASTM International. Standard Test Method for Knoop and Vickers Hardness of Materials (Designation: E384 – 11) 2015.
- [25] Suga Y, Miyakawa S, Ogawa K. Estimation of temperature distribution in the friction weld of carbon steel by the finite element method. *Weld Int* 1999;13:262–9. <https://doi.org/10.1080/09507119909447375>.
- [26] Li W, Vairis A, Preuss M, Ma T. Linear and rotary friction welding review. *Int Mater Rev* 2016;61:71–100. <https://doi.org/10.1080/09506608.2015.1109214>.
- [27] Nagode A, Resnik A, Vertnik R, Bizjak M, Kosec B, Gojić M, et al. The development of a banded microstructure in S355J2 steel bar. *Kov Mater* 2017;55:51–6. <https://doi.org/10.4149/km-2017-1-51>.
- [28] Piekarska W, Goszczyńska-Króliszewska D. Analytical Methods of Predicting the Structure and Mechanical Properties of High Tensile Strength Steel. *Procedia Eng* 2017;177:92–8. <https://doi.org/10.1016/j.proeng.2017.02.189>.
- [29] Kurt B, Orhan N, Ozel S. Interface microstructure of diffusion bonded austenitic stainless steel and medium carbon steel couple. *Sci Technol Weld Join* 2007;12:197–201. <https://doi.org/10.1179/174329307X175164>.
- [30] Madhusudan Reddy G, Srinivasa Rao K. Microstructure and mechanical properties of similar and dissimilar stainless steel electron beam and friction welds. *Int J Adv Manuf Technol* 2009;45:875–88. <https://doi.org/10.1007/s00170-009-2019-6>.
- [31] Shakil M, Ahmad M, Tariq NH, Hasan BA, Akhter JI, Ahmed E, et al. Microstructure and hardness studies of electron beam welded Inconel 625 and stainless steel 304L. *Vacuum* 2014;110:121–6. <https://doi.org/10.1016/j.vacuum.2014.08.016>.
- [32] MatWeb Material Property Data. No Title. Ovako S355J2 S355J2(M) Steel, +AR n.d. <http://www.matweb.com/search/datasheet.aspx?matguid=3c36b268408a4cc1ae7f789bd605d6c6&ckck=1>.
- [33] Materials A. No Title. Stainl Steel - Grade 316 (UNS S31600) n.d. <https://www.azom.com/properties.aspx?ArticleID=863>.
- [34] He W, Liu J, Sun S, Chen H, Guo H. Hot deformation behaviour and hot processing map of 316ln-nb stainless steel. *Mater Res Innov* 2011;15. <https://doi.org/10.1179/143307511X12858957673671>.
- [35] Sun C, Xiang Y, Zhou Q, Politis DJ, Sun Z, Wang M. Dynamic recrystallization and hot workability of 316LN stainless steel. *Metals (Basel)* 2016;6:1–13. <https://doi.org/10.3390/met6070152>.